



ARL-TR-7332 • JULY 2015



# Effects of Turbulence Model on Prediction of Hot-Gas Lateral Jet Interaction in a Supersonic Crossflow

by James DeSpirito

Approved for public release; distribution is unlimited.

## **NOTICES**

### **Disclaimers**

The findings in this report are not to be construed as an official Department of the Army position unless so designated by other authorized documents.

Citation of manufacturer's or trade names does not constitute an official endorsement or approval of the use thereof.

Destroy this report when it is no longer needed. Do not return it to the originator.



# Effects of Turbulence Model on Prediction of Hot-Gas Lateral Jet Interaction in a Supersonic Crossflow

by James DeSpirito

*Weapons and Materials Research Directorate, ARL*

REPORT DOCUMENTATION PAGE				Form Approved OMB No. 0704-0188	
<p>Public reporting burden for this collection of information is estimated to average 1 hour per response, including the time for reviewing instructions, searching existing data sources, gathering and maintaining the data needed, and completing and reviewing the collection information. Send comments regarding this burden estimate or any other aspect of this collection of information, including suggestions for reducing the burden, to Department of Defense, Washington Headquarters Services, Directorate for Information Operations and Reports (0704-0188), 1215 Jefferson Davis Highway, Suite 1204, Arlington, VA 22202-4302. Respondents should be aware that notwithstanding any other provision of law, no person shall be subject to any penalty for failing to comply with a collection of information if it does not display a currently valid OMB control number.</p> <p><b>PLEASE DO NOT RETURN YOUR FORM TO THE ABOVE ADDRESS.</b></p>					
1. REPORT DATE (DD-MM-YYYY) July 2015		2. REPORT TYPE Final		3. DATES COVERED (From - To) February 2014–December 2014	
4. TITLE AND SUBTITLE Effects of Turbulence Model on Prediction of Hot-Gas Lateral Jet Interaction in a Supersonic Crossflow				5a. CONTRACT NUMBER	
				5b. GRANT NUMBER	
				5c. PROGRAM ELEMENT NUMBER	
6. AUTHOR(S) James DeSpirito				5d. PROJECT NUMBER AH80	
				5e. TASK NUMBER	
				5f. WORK UNIT NUMBER	
7. PERFORMING ORGANIZATION NAME(S) AND ADDRESS(ES) US Army Research Laboratory ATTN: RDRL-WML-E Aberdeen Proving Ground, MD 21005-5066				8. PERFORMING ORGANIZATION REPORT NUMBER ARL-TR-7332	
9. SPONSORING/MONITORING AGENCY NAME(S) AND ADDRESS(ES)				10. SPONSOR/MONITOR'S ACRONYM(S)	
				11. SPONSOR/MONITOR'S REPORT NUMBER(S)	
12. DISTRIBUTION/AVAILABILITY STATEMENT Approved for public release; distribution is unlimited.					
13. SUPPLEMENTARY NOTES					
14. ABSTRACT <p>Computational fluid dynamic predictions of surface pressures resulting from lateral jet injection into a Mach 3 supersonic crossflow from a cone-cylinder-flare missile are compared with wind tunnel data. Predictions of a sonic, multispecies, hot-gas jet using real-gas methodology are compared with predictions of a cold-gas jet and a hot, nonreacting jet using the ideal-gas assumption. An evaluation of 9 turbulence models is performed to determine their ability to accurately predict the surface pressures due to the jet interaction flowfield resulting from the injection of the lateral jets into the Mach 3 crossflow. Predictions of axial and circumferential pressure profiles were found to be very dependent on turbulence models, with some models performing relatively poorly. Menter's Shear Stress Transport model gave very good predictions for the hot-gas and hot-air jets, while Menter's Baseline model provided the most accurate predictions for a cold-air jet. The study found that even with the observed variations in surface pressure, the aerodynamic forces and moments produced by the lateral jet interactions with the crossflow were much less sensitive to the turbulence model than were the surface pressure profiles. The ideal-gas hot-air jet was found to represent the multispecies, hot-gas jet reasonably well, making it a viable substitution for a real-gas solution under certain assumptions.</p>					
15. SUBJECT TERMS lateral jet, computational fluid dynamics, aerodynamics, jet interaction, crossflow					
16. SECURITY CLASSIFICATION OF:			17. LIMITATION OF ABSTRACT  UU	18. NUMBER OF PAGES  60	19a. NAME OF RESPONSIBLE PERSON James DeSpirito
a. REPORT Unclassified	b. ABSTRACT Unclassified	c. THIS PAGE Unclassified			19b. TELEPHONE NUMBER (include area code) 410-306-0778

## Contents

---

<b>List of Figures</b>	<b>iv</b>
<b>List of Tables</b>	<b>vi</b>
<b>Acknowledgments</b>	<b>vii</b>
<b>1. Introduction</b>	<b>1</b>
<b>2. Approach</b>	<b>2</b>
2.1 Cone-Cylinder-Flare Missile Model	2
2.2 Computational Details	3
2.2.1 Computational Domains	3
2.2.2 CFD Solver	5
2.2.3 Flow and Boundary Conditions	6
2.3 Jet Amplification Factors	7
<b>3. Results and Discussion</b>	<b>8</b>
3.1 Cold-Air Jet	9
3.2 Hot-Gas Jet	18
3.3 Hot-Air Jet	26
3.4 Comment on Turbulence Models	31
<b>4. Summary and Conclusions</b>	<b>33</b>
<b>5. References and Notes</b>	<b>34</b>
<b>Appendix A. Cold-Air Jet Turbulence Effects, <math>PR = 130</math></b>	<b>37</b>
<b>Appendix B. Hot-Gas Jet Turbulence Effects, <math>PR = 130</math></b>	<b>41</b>
<b>List of Symbols, Abbreviations, and Acronyms</b>	<b>45</b>
<b>Distribution List</b>	<b>48</b>

## List of Figures

Fig. 1	Cone-cylinder-flare wind tunnel model with jet nozzle .....	3
Fig. 2	Cone-cylinder-flare model with mesh: (a) full-domain, on symmetry and outlet planes, (b) symmetry plane with nozzle and density boxes, and (c) symmetry plane in nozzle exit area .....	4
Fig. 3	Typical lateral jet interaction flowfield around a body of revolution; Mach contours on symmetry and outlet planes and $C_p$ contours on missile surfaces, SST turbulence model, $Re = 14 \times 10^6$ , $PR = 220$ .....	9
Fig. 4	Cold-air jet surface pressure profiles longitudinally along missile axis at (a) $\phi = 180^\circ$ , (b) $\phi = 150^\circ$ , (c) $\phi = 120^\circ$ , and (d) circumferentially at $X/D = 4.3$ , BSL turbulence model, $Re = 14 \times 10^6$ , $PR = 220$ .....	10
Fig. 5	Cold-air jet surface pressure profiles longitudinally along missile axis at (a) $\phi = 180^\circ$ , (b) $\phi = 150^\circ$ , (c) $\phi = 120^\circ$ , and (d) circumferentially at $X/D = 4.3$ , BSL turbulence model, $Re = 25 \times 10^6$ , $PR = 130$ .....	11
Fig. 6	Effect of $k-\omega$ -based turbulence models on cold-air jet surface pressure profiles longitudinally along missile axis at (a) $\phi = 180^\circ$ , (b) $\phi = 150^\circ$ , (c) $\phi = 120^\circ$ , and (d) circumferentially at $X/D = 4.3$ , $Re = 14 \times 10^6$ , $PR = 220$ .....	13
Fig. 7	Effect of BSL and $k-\varepsilon$ -based turbulence models on cold-air jet surface pressure profiles longitudinally along missile axis at (a) $\phi = 180^\circ$ , (b) $\phi = 150^\circ$ , (c) $\phi = 120^\circ$ , and (d) circumferentially at $X/D = 4.3$ , $Re = 14 \times 10^6$ , $PR = 220$ .....	14
Fig. 8	Effect of BSL and SA-based turbulence models on cold-air jet surface pressure profiles longitudinally along missile axis at (a) $\phi = 180^\circ$ , (b) $\phi = 150^\circ$ , (c) $\phi = 120^\circ$ , and (d) circumferentially at $X/D = 4.3$ , $Re = 14 \times 10^6$ , $PR = 220$ .....	15
Fig. 9	Hot-gas jet surface pressure profiles longitudinally along missile axis at (a) $\phi = 180^\circ$ , (b) $\phi = 150^\circ$ , (c) $\phi = 120^\circ$ , and (d) circumferentially at $X/D = 4.3$ , SST turbulence model, $Re = 14 \times 10^6$ , $PR = 220$ .....	19
Fig. 10	Hot-gas jet surface pressure profiles longitudinally along missile axis at (a) $\phi = 180^\circ$ , (b) $\phi = 150^\circ$ , (c) $\phi = 120^\circ$ , and (d) circumferentially at $X/D = 4.3$ , SST turbulence model, $Re = 25 \times 10^6$ , $PR = 130$ .....	20
Fig. 11	Effect of $k-\omega$ -based turbulence models on hot-gas jet surface pressure profiles longitudinally along missile axis at (a) $\phi = 180^\circ$ , (b) $\phi = 150^\circ$ , (c) $\phi = 120^\circ$ , and (d) circumferentially at $X/D = 4.3$ , $Re = 14 \times 10^6$ , $PR = 220$ .....	22

Fig. 12	Effect of SST and $k$ - $\varepsilon$ -based turbulence models on hot-gas jet surface pressure profiles longitudinally along missile axis at (a) $\phi = 180^\circ$ , (b) $\phi = 150^\circ$ , (c) $\phi = 120^\circ$ , and (d) circumferentially at $X/D = 4.3$ , $Re = 14 \times 10^6$ , $PR = 220$ .....	23
Fig. 13	Effect of SST and SA-based turbulence models on hot-gas jet surface pressure profiles longitudinally along missile axis at (a) $\phi = 180^\circ$ , (b) $\phi = 150^\circ$ , (c) $\phi = 120^\circ$ , and (d) circumferentially at $X/D = 4.3$ , $Re = 14 \times 10^6$ , $PR = 220$ .....	24
Fig. 14	Surface pressure profiles longitudinally along missile axis at (a) $\phi = 180^\circ$ , (b) $\phi = 150^\circ$ , (c) $\phi = 120^\circ$ , and (d) circumferentially at $X/D = 4.3$ , SST turbulence model, $Re = 14 \times 10^6$ , $PR = 220$ .....	27
Fig. 15	Surface pressure profiles longitudinally along missile axis at (a) $\phi = 180^\circ$ , (b) $\phi = 150^\circ$ , (c) $\phi = 120^\circ$ , and (d) circumferentially at $X/D = 4.3$ , SST turbulence model, $Re = 25 \times 10^6$ , $PR = 130$ .....	28
Fig. 16	Mach contours on symmetry plane and $C_p$ contours on missile surface (a, c, e) and simulated surface oil flow streamlines and $C_p$ contours on missile surface (b, d, f) for (a, b) cold-air, (c, d) hot-air, and (e, f) hot-gas jets; SST turbulence model, $Re = 14 \times 10^6$ , $PR = 220$ .....	31
Fig. A-1	Effect of $k$ - $\omega$ -based turbulence models on cold-air jet surface pressure profiles longitudinally along missile axis at (a) $\phi = 180^\circ$ , (b) $\phi = 150^\circ$ , (c) $\phi = 120^\circ$ , and (d) circumferentially at $X/D = 4.3$ , $Re = 14 \times 10^6$ , $PR = 130$ .....	38
Fig. A-2	Effect of Menter's baseline (BSL) and $k$ - $\varepsilon$ -based turbulence models on cold-air jet surface pressure profiles longitudinally along missile axis at (a) $\phi = 180^\circ$ , (b) $\phi = 150^\circ$ , (c) $\phi = 120^\circ$ , and (d) circumferentially at $X/D = 4.3$ , $Re = 14 \times 10^6$ , $PR = 130$ .....	39
Fig. A-3	Effect of BSL and Spalart-Allmaras-based turbulence models on cold-air jet surface pressure profiles longitudinally along missile axis at (a) $\phi = 180^\circ$ , (b) $\phi = 150^\circ$ , (c) $\phi = 120^\circ$ , and (d) circumferentially at $X/D = 4.3$ , $Re = 14 \times 10^6$ , $PR = 130$ .....	40
Fig. B-1	Effect of $k$ - $\omega$ -based turbulence models on hot-gas jet surface pressure profiles longitudinally along missile axis at (a) $\phi = 180^\circ$ , (b) $\phi = 150^\circ$ , (c) $\phi = 120^\circ$ , and (d) circumferentially at $X/D = 4.3$ , $Re = 14 \times 10^6$ , $PR = 130$ .....	42
Fig. B-2	Effect of Menter's Shear Stress Transport (SST) and $k$ - $\varepsilon$ -based turbulence models on hot-gas jet surface pressure profiles longitudinally along missile axis at (a) $\phi = 180^\circ$ , (b) $\phi = 150^\circ$ , (c) $\phi = 120^\circ$ , and (d) circumferentially at $X/D = 4.3$ , $Re = 14 \times 10^6$ , $PR = 130$ .....	43
Fig. B-3	Effect of SST and Spalart-Allmaras-based turbulence models on hot-gas jet surface pressure profiles longitudinally along missile axis at (a) $\phi = 180^\circ$ , (b) $\phi = 150^\circ$ , (c) $\phi = 120^\circ$ , and (d) circumferentially at $X/D = 4.3$ , $Re = 14 \times 10^6$ , $PR = 130$ .....	44

## List of Tables

---

Table 1	Wind tunnel crossflow and jet boundary conditions.....	5
Table 2	Summary of turbulence model effects for cold-air jet, $Re = 14 \times 10^6$ , $PR = 220$ .....	16
Table 3	Summary of turbulence model effects for cold-air jet, $Re = 25 \times 10^6$ , $PR$ $= 130$ .....	17
Table 4	Summary of turbulence model effects for hot-gas jet, $Re = 14 \times 10^6$ , $PR = 220$ .....	25
Table 5	Summary of turbulence model effects for hot-gas jet, $Re = 25 \times 10^6$ , $PR = 130$ .....	26
Table 6	Summary of turbulence model effects for hot-air jet, $Re = 14 \times 10^6$ , $PR = 220$ .....	29
Table 7	Summary of turbulence model effects for hot-air jet, $Re = 25 \times 10^6$ , $PR = 130$ .....	30



## **Acknowledgments**

---

The author thanks Dr Sidra I Siltan for reviewing this manuscript. This work was supported in part by a grant of high-performance computing time from the US Department of Defense (DOD) High Performance Computing Modernization program at the US Army Research Laboratory DOD Supercomputing Resource Center (DSRC), Aberdeen Proving Ground, MD, and the Air Force DOD DSRC, Wright-Patterson Air Force Base, OH.

INTENTIONALLY LEFT BLANK.

## 1. Introduction

---

Jets issuing into a crossflow commonly occur in both nature (e.g., volcano and fire plumes) and engineering technology (e.g., gas-turbine fuel injection and aerodynamic divert thrusters).<sup>1,2</sup> A lateral reaction jet is one type of aerodynamic divert thruster used for maneuver control of a missile or projectile. However, instead of just the force of the jet thrust, as would occur in a vacuum, the operation of a lateral reaction jet in the atmosphere leads to an interference flow between the jet plume and the flow over the vehicle that produces an additional jet interaction (JI) force. This JI force can have a significant effect on the resulting forces and moments imparted by the jet onto the vehicle. The jet thrust may be either attenuated or amplified depending on the jet nozzle location along the body. In addition, the effective location at which the force acts is usually also moved away from the jet exit nozzle.<sup>3-5</sup> Accurate prediction of the JI force and its effective point of action are critical to the accuracy of any flight trajectory simulations using an aerodynamic model based on these predictions.

The availability of new validation data on bodies of revolution that provide both surface pressure and force and moment data is somewhat limited. Wind tunnel data gathering surface pressure, oil flow, and perhaps particle image velocimetry data is very useful, but usually does not also include the forces and moments on the model. Also, for practical reasons at the wind tunnel test facility, the data are usually taken with a single-species cold-gas jet (i.e., facility room temperature) rather than a multispecies gas at the flame temperature of the combustion products of the gas generator. If flight test data are available, only force and moment data may be extracted, which can also be difficult to accurately determine from the flight test data.

One series of experimental data appropriate for validation of computational fluid dynamics (CFD) simulations was published by researchers from the French-German Research Institute of Saint-Louis (ISL) in Saint-Louis, France<sup>6-8</sup> and the German Aerospace Center (DLR) in Braunschweig, Germany.<sup>7-10</sup> These studies involved wind tunnel investigations of radial cold-gas ejection from 1–3 sonic nozzles on a cone-cylinder-flare (CCF) missile in supersonic crossflows of Mach 2.8 and 3.0. Jet pressure ratios ( $PR$ s) of 50–300 were investigated, and data included wall surface pressures, measured from pressure taps arranged in 4 longitudinal sections and up to 4 circumferential sections, in addition to some oil-flow visualizations.

More recent results from these authors include additional results from wind tunnel investigations on hot-gas lateral jet ejection<sup>11,12</sup> and an experimental and computational study on the substitution of hot-gas lateral jets by cold-gas simulants in supersonic flow.<sup>13</sup> Hold et al.<sup>14</sup> performed a computational investigation based on the experimental data of Stahl et al.,<sup>11</sup> finding that it was necessary to use a real-gas, nonreacting, multispecies-based solution to most accurately predict the missile surface pressures due to the JI. However, Hold et al.<sup>14</sup> also found that an ideal-gas hot-air jet provided reasonable aerodynamic force and moment predictions compared with the multispecies hot-gas predictions.

DeSpirito<sup>15</sup> recently investigated the effect of turbulence model on cold-gas lateral jet injection using the experimental data of ISL and DLR for validation.<sup>6–10</sup> He found that very good to excellent predictions of the missile surface pressure in the longitudinal and circumferential planes of the jet nozzle were achieved using Menter’s Baseline (BSL) turbulence model. DeSpirito also found that, even with sometimes significant variations in the surface pressure induced by the JI, the variation of the induced aerodynamic forces and moments were much less sensitive to the turbulence model.

The objective of the present study is to extend the cold-gas lateral jet injection turbulence model investigation<sup>15</sup> to include the effects of (nonreacting) multispecies hot-gas injection. The data of Stahl et al.<sup>11,12</sup> is used to validate the numerical predictions of surface pressure profiles resulting from the interaction of the jet with the supersonic crossflow. The results are also compared with the computations of Hold et al.<sup>14</sup>

## **2. Approach**

---

### **2.1 Cone-Cylinder-Flare Missile Model**

---

The cone-cylinder-flare model shown in Fig. 1 consisted of a  $2.8D$ -long conical nose ( $D = 90$  mm), a  $3.2D$ -long cylindrical section, and a  $3D$ -long flared afterbody with a  $1.66D$  base diameter. The jet nozzle (red circle in Fig. 1) was a circular, sonic nozzle of diameter  $d = 4.6$  mm ( $0.05D$ ) located on the cylindrical section at a position  $4.3D$  from the nose at a circumferential angle of  $\phi = 180^\circ$ . The circumferential angles were measured clockwise around the missile when viewed from the rear with the  $0^\circ$  position at the bottom. The wind tunnel model<sup>11,12</sup> contained 93 static surface pressure taps of diameter 0.5 mm; 83 pressure tapes were positioned in 3 longitudinal sections at circumferential angles of  $\phi = 180^\circ$ ,

150°, and 120°, and 10 taps at  $X/D = 4.3$  in an angle range of  $190^\circ \leq \phi \leq 270^\circ$ . The longitudinal taps extended from approximately  $3.5 \leq X/D \leq 6.0$ , as indicated by the white lines in Fig. 1.

The experimental data from Stahl et al.<sup>11</sup> and the numerical data from Hold et al.<sup>14</sup> were digitized by the author for direct comparisons with CFD predictions.

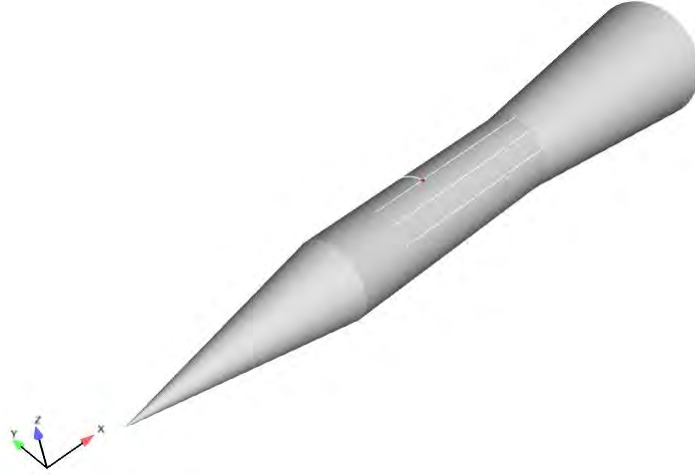


**Fig. 1 Cone-cylinder-flare wind tunnel model with jet nozzle**

## 2.2 Computational Details

---

### 2.2.1 Computational Domains

The computational domain of the CCF model was the same as that used for the freestream version of the mesh in the cold-gas simulations<sup>15</sup> and is shown in Fig. 2. Only one-half of the domain was modeled, taking advantage of the symmetry of the geometry. The computational domains were meshed with MIME from Metacomp Technologies.<sup>16</sup> The forward surface of the domain was a conical section located  $0.5 D$  in front of the missile nose, and the downstream section ended at the end of the flare section of the missile. The outer radial surface was located  $5 D$  from the missile axis. Mesh density boxes were used to refine the mesh in the region of the jet nozzle and further downstream. A cylindrical jet nozzle the same length as in the experiment was included in the computational domain (Figs. 2b and 2c).

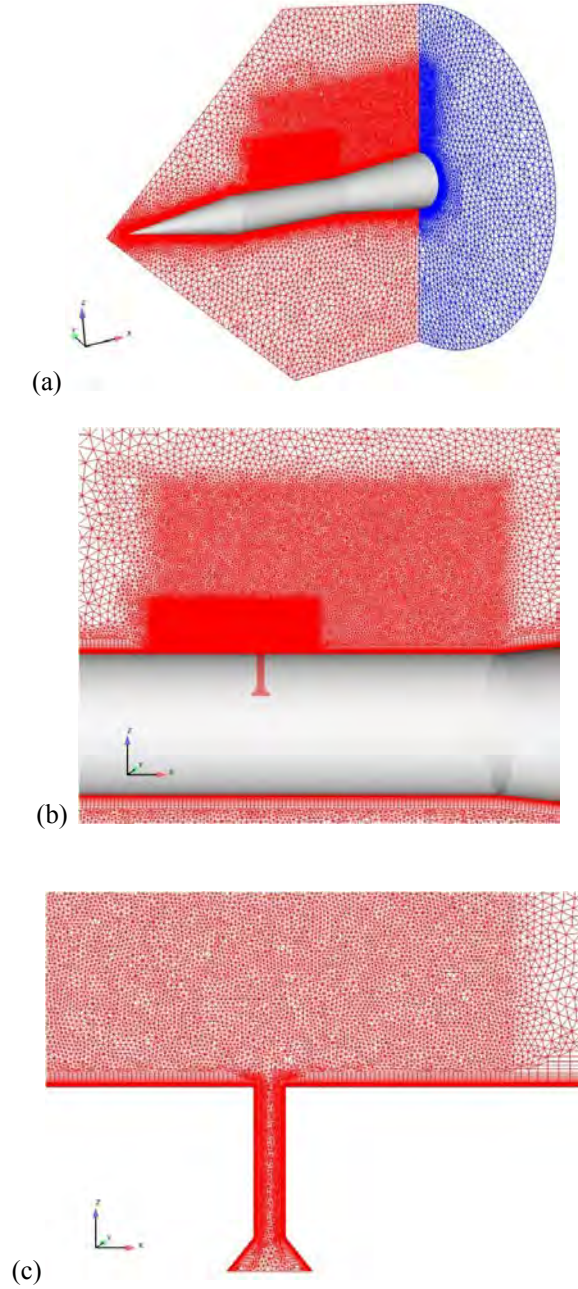


**Fig. 2 Cone-cylinder-flare model with mesh: (a) full-domain, on symmetry and outlet planes, (b) symmetry plane with nozzle and density boxes, and (c) symmetry plane in nozzle exit area**

The total mesh size was approximately 12.0 M cells and was previously validated as adequate.<sup>15</sup> Prism layers were used along all solid boundaries, including the nozzle wall, with the first cell wall spacing set to  $1 \times 10^{-6}$  m. The missile surfaces were modeled using the “solve-to-wall” methodology with  $y^+$  values less than 1.0 on the body and flare sections. The  $y^+$  values on the conical nose for the higher

Reynolds number case (Table 1) peaked at about 1.25. The  $y^+$  values can be much larger on the nozzle exit wall due to the much different flow properties there from the gas expansion. Therefore, the nozzle wall was modeled with an advanced 2-layer wall function boundary condition that reverts to a solve-to-wall method where the mesh is fine enough, or else to a wall function as appropriate.

**Table 1 Wind tunnel crossflow and jet boundary conditions**

$M$	$Re$ ( $\times 10^6$ )	$T_\infty$ (K)	$T_0$ (K)	$p_\infty$ (kPa)	$p_0$ (MPa)	$\rho_\infty$ (kg/m <sup>3</sup> )	$T_{0jH}$ (K)	$T_{0jC}$ (K)	$P_{0j}$ (MPa)	$PR$
3.0	14	104.6	293.	54.5	2.0	1.82	2300.	244.	12.	220
3.0	25	104.6	293.	92.3	3.4	3.07	2300.	244.	12.	130

### 2.2.2 CFD Solver

The commercially available CFD<sup>++</sup> code,<sup>17</sup> version 14.1, was used in this study. The 3-dimensional, compressible, Reynolds-averaged Navier-Stokes (RANS) equations are solved using a finite volume method. A point-implicit time-integration scheme with local time-stepping, defined by the Courant-Friedrichs-Lewy number, was used to advance the solution toward steady-state. The multigrid W-cycle method with a maximum of 4 cycles and a maximum of 20 grid levels was used to accelerate convergence. Implicit temporal smoothing was applied for increased stability, which is especially useful where strong transients arise. The inviscid flux function was a second-order upwind scheme using a Harten-Lax-van Leer-Contact Riemann solver and a multidimensional Total-Variation-Diminishing continuous flux limiter.<sup>17</sup> The compressible, perfect-gas solver was used for the single-species (air) simulations, while the real-gas solver was used for the hot-gas multispecies simulations. All simulations were double precision.

The choice of turbulence model is a key factor in the numerical modeling of complex flows such as this. CFD<sup>++</sup> has available a large set of turbulence models, 9 of which were investigated for their accuracy in prediction of the surface pressure profiles. The models investigated in this study were 1) Menter's  $k-\omega$  Shear Stress Transport (SST) 2-equation model,<sup>18</sup> 2) Menter's BSL 2-equation model,<sup>18</sup> 3) the standard<sup>19</sup> (kw) and 4) realizable<sup>17</sup>  $k-\omega$  (rkw) 2-equation models, 5) the Spalart-Allmaras's (SA) 1-equation model,<sup>20</sup> 6) the SA 1-equation model with rotation/curvature correction (SARC),<sup>21</sup> 7) the realizable  $k-\varepsilon$  (rke) 2-equation model,<sup>22</sup> 8) the cubic  $k-\varepsilon$  (cke) nonlinear 2-equation model,<sup>23</sup> and 9) Goldberg's  $k-\varepsilon-R_t$  (keR) 3-equation model.<sup>24</sup> The compressibility correction was used in all cases.

The simulations were performed on an IBM iDataPlex (PERSHING) supercomputer at the US Army Research Laboratory (ARL) Department of Defense (DOD) Supercomputing Resource Center (DSRC) at Aberdeen Proving Ground, MD, and SGI ICE X (SPIRIT) and Cray XC30 (LIGHTNING) supercomputers at the US Air Force DOD DSRC at Wright-Patterson Air Force Base, OH.

### 2.2.3 Flow and Boundary Conditions

The pressure and temperature conditions for the study were obtained from the experiments conducted by Stahl et al.<sup>11,12</sup> and are summarized in Table 1. The turbulence values were those used in the previous study<sup>15</sup>:  $I_t = 0.5\%$  and  $l_t = 2$  mm. All tests in the wind tunnel were performed at  $\alpha = 0^\circ$ . The higher Reynolds number (lower  $PR$ ) case corresponds to the jet injecting into a 1.7 times denser fluid due to the higher crossflow pressure.

The experiment included both a cold-gas jet and a hot multispecies gas jet, labeled here as “cold-air” and “hot-gas.” As done by Hold et al.,<sup>14</sup> an additional case (labeled “hot-air”) was simulated using air at the temperature of the hot multispecies gas. This hot-air case is likely the one a researcher would simulate if an ideal-gas solver rather than a real-gas solver was used, so the comparison with the multispecies hot-gas results is important. The cold gas was set to a total temperature of 244 K, while both the hot jets were set to a total temperature of 2,300 K, the expected combustion chamber temperature. Stahl et al.<sup>11,12</sup> give the jet temperature as 2,058 K at the nozzle exit. Probing of the nozzle in the CFD results gave the jet exit temperature in the range of 2,050–2,072 K, indicating that the chosen jet total temperature was appropriate.

All solid surfaces were modeled as no-slip, adiabatic walls with solve-to-wall methodology on the missile body surfaces and wall functions on the nozzle wall for the reasons described in Section 2.2.1. A symmetry boundary condition was used on the symmetry plane of the domain. The outer forward and radial boundaries were modeled using a characteristics-based inflow/outflow boundary condition, which is based on solving a Riemann problem at the boundary. The exit plane was modeled with a supersonic outflow boundary condition. The inlet to the nozzle was modeled as a subsonic reservoir boundary inflow with a specified total pressure and temperature ( $P_{0j}$  and  $T_{0jH}$  or  $T_{0jC}$ ). This procedure allows the nozzle exit conditions to be directly calculated during the solution.

The hot gas in the experiment was generated via a front-burning double-based solid propellant charge and was composed of 37.6% carbon dioxide ( $\text{CO}_2$ ) (mass ratio %), 1.7% hydrogen ( $\text{H}_2$ ), 1.1% lead ( $\text{Pb}$ ), 10.3% water ( $\text{H}_2\text{O}$ ), 34.9% carbon monoxide ( $\text{CO}$ ), 13.9% nitrogen ( $\text{N}_2$ ), and 0.3% copper ( $\text{Cu}$ ). Similar to Hold



et al.,<sup>14</sup> the present study used a jet consisting of only 5 of the 7 products listed, eliminating the Cu and Pb products. The mass fractions were 38.21% CO<sub>2</sub>, 1.73% H<sub>2</sub>, 10.47% H<sub>2</sub>O, 35.47% CO, and 14.12% N<sub>2</sub>. Air was used for the crossflow gas in the present study, while Hold et al. used O<sub>2</sub> and N<sub>2</sub>. Several simulations were completed to investigate the effects of these small variations on the resulting pressure traces and product gas properties; the effects were found to be minimal. The predicted isentropic exponent and gas constant for the multispecies gas were  $\gamma = 1.233$  and  $R_H = 339$  J/kg-K. These compare reasonably well to the experimental values reported by Stahl et al.<sup>12</sup> of  $\gamma = 1.235$  and  $R_H = 319$  J/kg-K.

The jet thrust is calculated by taking the difference between the computed forces on the total pressure boundary at the bottom of the plenum and the remaining plenum and the jet nozzle walls. These forces are calculated using the same tool available within CFD<sup>++</sup> used to calculate the forces and moments on the other surfaces. Another method within CFD<sup>++</sup> is to define a plane at the exit of the nozzle and use that same tool to calculate the forces and fluxes on that plane. These methods can be more accurate than using the standard thrust equation, which requires some average value of the static and dynamic pressures at the jet exit.

### 2.3 Jet Amplification Factors

---

The jet amplification factor is a measure of the effect that the JI has on the control forces and moments or the “efficiency” of the jet. The jet force and moment amplification factors are defined as

$$K_f = \frac{F_j + F_{ji}}{F_j}, \quad (1)$$

and

$$K_m = \frac{M_j + M_{ji}}{M_j}. \quad (2)$$

An amplification factor greater than one indicates the JI effect increases the effectiveness of the jet thrust force,  $F_j$ , or the moment induced by the jet thrust,  $M_j = F_j l_j$ . If the body, such as a projectile or missile, is at an angle of attack, the force or moment induced by the angle of attack—with the jet off—is subtracted from that resulting with the jet on, e.g.,

$$F_{ji} = F_{\text{total}} - F_{\text{no-jet}} - F_j, \quad (3)$$

where  $F_{\text{total}}$  is total force due to the jet thrust, JI effects, and angle of attack.  $F_{\text{no-jet}}$  is the aerodynamic force in the absence of the jet, which will be nonzero when  $\alpha \neq 0^\circ$ . Moments due to these forces follow directly, and the equations using coefficients are similar. On a flat plate or a projectile at  $0^\circ$  angle of attack, the JI

force and moment are computed directly, since there is no force normal to the surface with the jet off. Following Gnemmi and Schafer,<sup>6</sup> if the jet nozzle axis is located near the center of gravity, the moment amplification factor is redefined as

$$K_m = 1 + \frac{M_{ji}}{F_j D} \quad (4)$$

since the jet moment,  $M_j = F_j l_j$ , goes to zero as the jet axis location approaches the center of gravity location.

### 3. Results and Discussion

---

Figure 3 shows a typical flowfield resulting from a lateral jet injection into a supersonic crossflow.<sup>1,2</sup> A description of the flowfield will help in understanding some of the features in the surface pressure profiles presented in later sections. The particular case in Fig. 3 is a multispecies hot-gas simulation using the SST turbulence model for  $Re = 14 \times 10^6$  and  $PR = 220$ . The jet is located behind a bow shock formed at the nose of the missile. A second “jet bow shock” forms in front of the jet due the obstruction; the shock-boundary layer interaction leads to flow separation and the formation of a  $\lambda$ -shock structure. Two counter-rotating horseshoe vortices (not shown) emanate from the forward separation region. The jet bow shock and horseshoe vortices wrap around the missile body as they traverse rearward (indicated by high- and low-pressure bands). A barrel shock surrounds the jet plume and terminates in a Mach disk. The most dominant feature is usually a counter-rotating vortex pair formed by the jet wake as it travels downstream.<sup>1,15</sup> There is usually a large region of low pressure on the missile surface in the jet wake region, which is followed by a recompression shock (end of dark blue region).

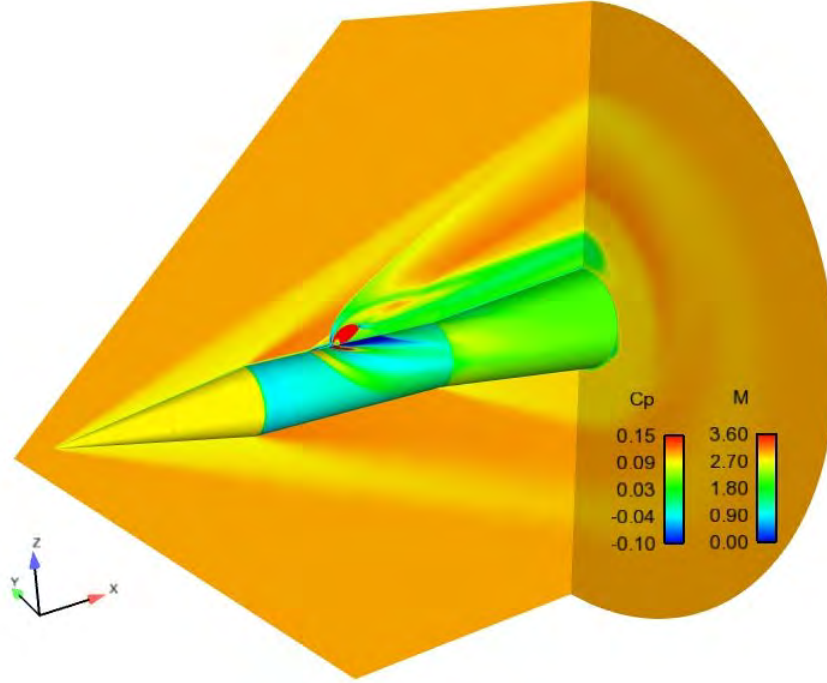


**Fig. 3** Typical lateral jet interaction flowfield around a body of revolution; Mach contours on symmetry and outlet planes and  $C_p$  contours on missile surfaces, SST turbulence model,  $Re = 14 \times 10^6$ ,  $PR = 220$

### 3.1 Cold-Air Jet

The cold-air lateral jets have different properties from those that were simulated in DeSpirito<sup>15</sup>: a smaller jet-to-missile diameter ratio (0.05 vs. 0.1) and higher wind tunnel freestream pressures ( $\geq 55$  kPa vs.  $\leq 21$  kPa), which leads to much higher tunnel freestream densities for similar values of  $PR$ . As the BSL turbulence model performed best in the simulations of DeSpirito<sup>15</sup>, it was chosen as the primary model in the initial simulations for this study. Figures 4 and 5 show the predicted and measured pressure profiles at  $PR = 220$  ( $Re = 14 \times 10^6$ ) and  $PR = 130$  ( $Re = 25 \times 10^6$ ), respectively. The pressure data is presented in terms of  $\Delta C_p = C_p - C_{p_{no-jet}}$ , where the  $C_{p_{no-jet}}$  values were obtained from single simulations at each  $PR$  using the BSL turbulence model. The predictions at both  $PR$  are excellent at all longitudinal and the circumferential profile locations. The major features of the pressure profiles at all locations are captured, including the forward separation point, peak pressures in forward separation region, and the rearward recompression location and pressure magnitude. Hold et al.<sup>14</sup> also obtained very good results for this case using the SST turbulence model with the DLR TAU code,<sup>25</sup> and those results are also plotted in Figs. 4 and 5 for comparison. There are some minor differences between the ARL and the Hold et al. results but both compare well to the more limited experimental data points.

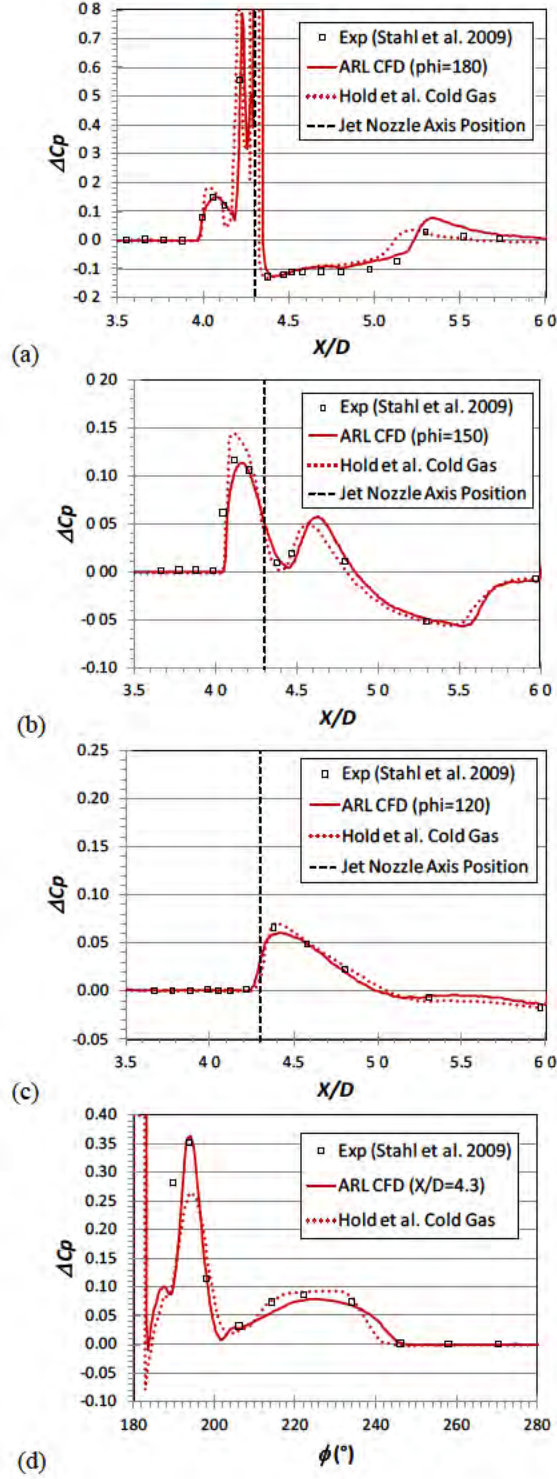


**Fig. 4** Cold-air jet surface pressure profiles longitudinally along missile axis at (a)  $\phi = 180^\circ$ , (b)  $\phi = 150^\circ$ , (c)  $\phi = 120^\circ$ , and (d) circumferentially at  $X/D = 4.3$ , BSL turbulence model,  $Re = 14 \times 10^6$ ,  $PR = 220$

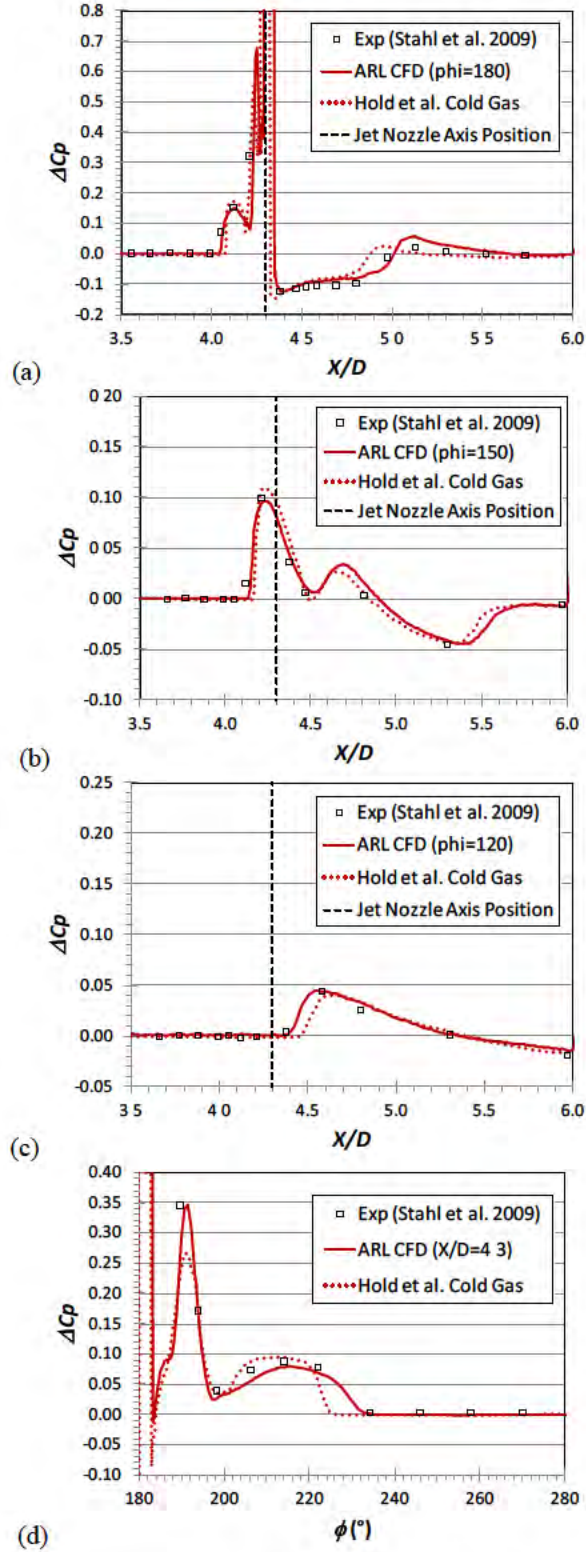
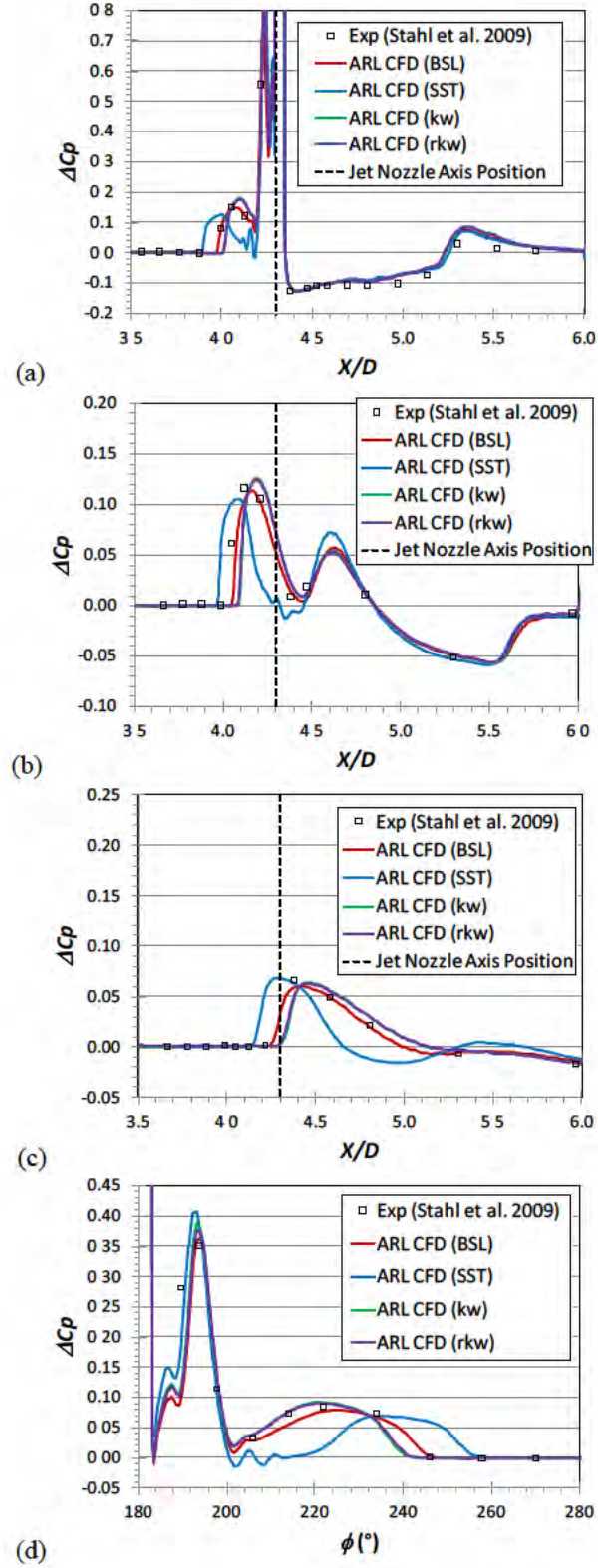


**Fig. 5** Cold-air jet surface pressure profiles longitudinally along missile axis at (a)  $\phi = 180^\circ$ , (b)  $\phi = 150^\circ$ , (c)  $\phi = 120^\circ$ , and (d) circumferentially at  $X/D = 4.3$ , BSL turbulence model,  $Re = 25 \times 10^6$ ,  $PR = 130$

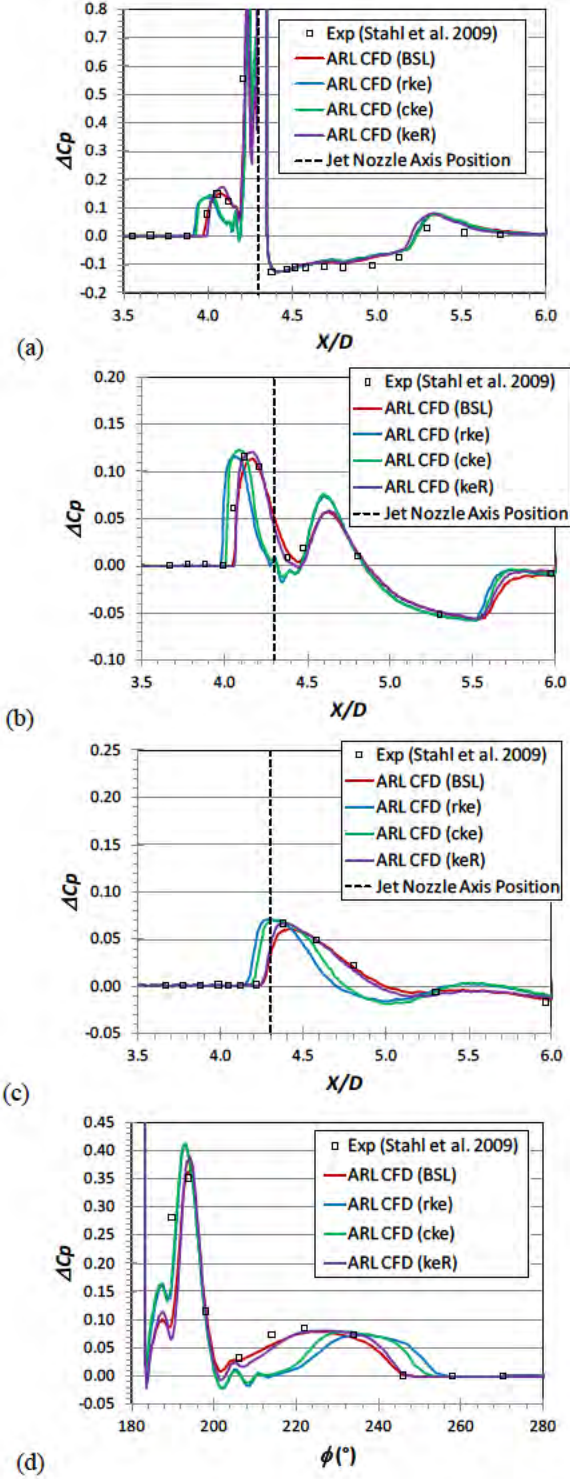
The other 8 turbulence models were run with the cold-air jet, and the results are compared in Figs. 6–8. Figure 6 shows the comparison of the BSL and the other  $k$ - $w$ -based turbulence models at the 3 longitudinal rows of ports and the circumferential row of ports for the  $PR = 220$  case. The SST model results did not compare as well, predicting earlier forward separation and lower peak pressure in this region (similar to the cold-air results reported in DeSpirito.<sup>15</sup> The  $kw$  and  $rkw$  model results are almost indistinguishable and provide reasonably good results, similar to the BSL model. It can be seen in Fig. 6 that the pressure profiles not in line with the jet ( $\phi \neq 180^\circ$ , Figs. 6b, 6c, and 6d) are very dependent on the features of the forward separation region in line with the jet (Fig. 6a). This is because the features of the  $\lambda$ -shock and jet bow shock ahead of the jet nozzle curve around the body and move rearward, and any change in the location of these forward features will translate into comparable differences at the other circumferential locations. For this reason, some of the following figures will only include the  $\phi = 180^\circ$  longitudinal and the circumferential profiles.

Figure 7 shows the comparisons of the BSL and  $k$ - $\varepsilon$ -based turbulence models, showing the  $rke$  and nonlinear  $cke$  models predict forward separation too early and overall compare more closely with the SST results (Fig. 6a–6d). The  $keR$  model provides reasonable results, similar to the BSL model. Figure 8 shows the comparison of the BSL and the SA-based models, which also compare reasonably well with the BSL model results. The SA model predicts the forward separation slightly more accurately than the SARC version of the model, which includes corrections for rotation and curvature in the flow. It may appear in Fig. 8d that the SARC model performs better in the circumferential profile, however, that is more likely due to the slightly delayed forward separation prediction impacting the downstream, out-of-jet-plane results. Similar results were found for the  $PR = 130$  case and the same models (BSL,  $kw$ ,  $rkw$ ,  $keR$ , SA, and SARC) again performed adequately in predicting the experimental pressure profiles. These results are presented in Appendix A.





**Fig. 6** Effect of  $k-\omega$ -based turbulence models on cold-air jet surface pressure profiles longitudinally along missile axis at (a)  $\phi = 180^\circ$ , (b)  $\phi = 150^\circ$ , (c)  $\phi = 120^\circ$ , and (d) circumferentially at  $X/D = 4.3$ ,  $Re = 14 \times 10^6$ ,  $PR = 220$



**Fig. 7** Effect of BSL and  $k$ - $\varepsilon$ -based turbulence models on cold-air jet surface pressure profiles longitudinally along missile axis at (a)  $\phi = 180^\circ$ , (b)  $\phi = 150^\circ$ , (c)  $\phi = 120^\circ$ , and (d) circumferentially at  $X/D = 4.3$ ,  $Re = 14 \times 10^6$ ,  $PR = 220$



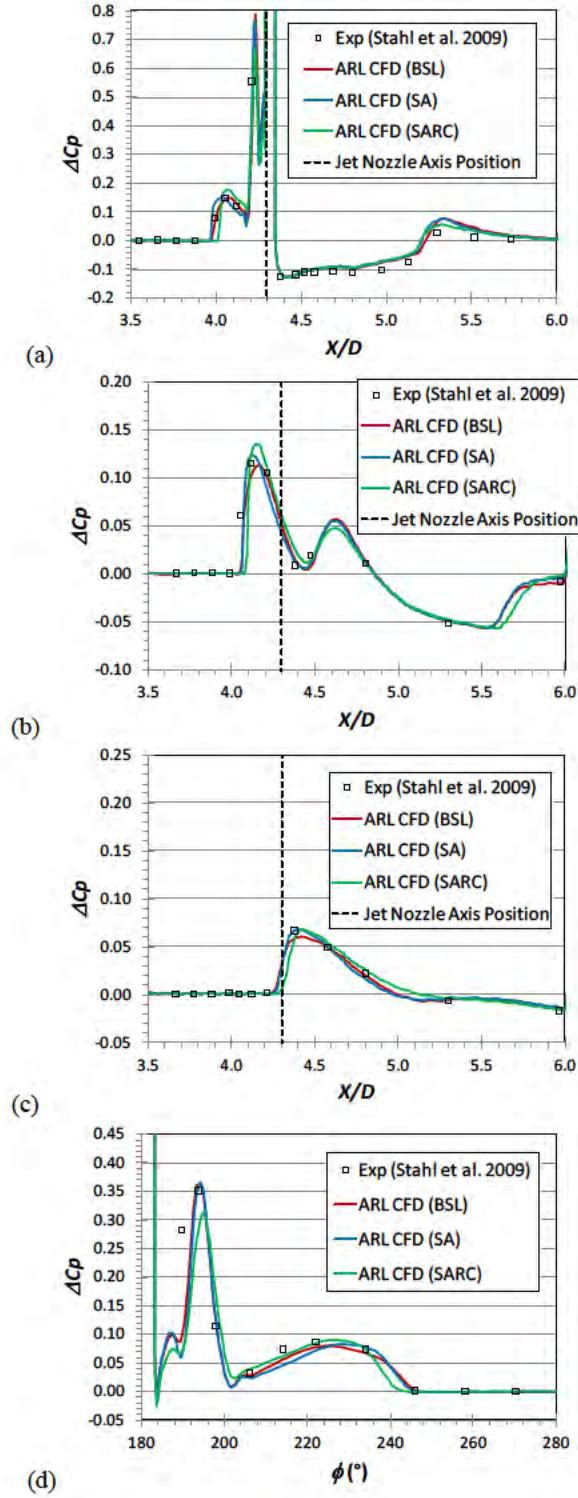


**Fig. 8** Effect of BSL and SA-based turbulence models on cold-air jet surface pressure profiles longitudinally along missile axis at (a)  $\phi = 180^\circ$ , (b)  $\phi = 150^\circ$ , (c)  $\phi = 120^\circ$ , and (d) circumferentially at  $X/D = 4.3$ ,  $Re = 14 \times 10^6$ ,  $PR = 220$

It is important to estimate how these differences in pressure profiles due to the chosen turbulence model translate into variation of aerodynamic forces and moments. Tables 2 and 3 summarize these results for the  $PR = 220$  and 130 cold-air cases, respectively. For each turbulence model, the tables list the resultant axial force, jet thrust force, JI force, moment about nose ( $X/D = 0$ ) due to jet thrust, moment about nose due to JI, and the JI moment about the jet nozzle location (taken as the moment reference point [MRP]). Also listed are the resultant force center of pressure and the amplification forces and moments. A positive force is in the “up” direction, so the jet thrust force is negative and would produce a positive, or “nose-up,” moment about the nose. Therefore, it is observed that the JI force is of significant amplitude and in the opposite direction as the thrust, leading to low force amplification values of 30% and 13% for  $PR = 220$  and 130, respectively. This positive JI force, with an effective center of pressure located behind the jet nozzle exit, produces a nose-down (negative) moment about both the nose and the jet nozzle exit location. This leads to the negative moment amplification values about the nose ( $K_{m(0)}$ , Eq. 2), which is opposite of the direction that would be due to the jet thrust in the absence of the JI force. These force amplification factors for the flare missile are much lower than those usually observed for a missile with tail fins. In the tail-fin case, the force amplification factors are usually about 70%–80%.<sup>3–5</sup>

**Table 2 Summary of turbulence model effects for cold-air jet,  $Re = 14 \times 10^6$ ,  $PR = 220$**

TM	$F_A$ (N)	$F_j$ (N)	$F_{ji}$ (N)	$M_{j(0)}$ (N-m)	$M_{ji(0)}$ (N-m)	$M_{ji}$ (N-m)	$X_{cp}/D$	$K_f$	$K_m$	$K_{m(0)}$
SST	236.2	-118.3	83.3	45.8	-58.6	-26.3	7.82	0.30	3.47	-0.28
BSL	240.6	-118.2	84.3	45.7	-57.8	-25.1	7.61	0.29	3.36	-0.26
kw	245.7	-118.2	81.7	45.7	-58.3	-26.6	7.92	0.31	3.50	-0.27
rkw	248.8	-118.2	81.4	45.7	-58.0	-26.5	7.92	0.31	3.50	-0.27
rke	241.4	-117.9	84.8	45.6	-58.6	-25.8	7.68	0.28	3.43	-0.28
cke	239.8	-117.9	84.2	45.6	-58.6	-26.0	7.73	0.29	3.45	-0.28
keR	245.2	-117.9	83.1	45.6	-58.5	-26.3	7.82	0.30	3.48	-0.28
SA	246.9	-118.0	82.6	45.6	-58.1	-26.2	7.82	0.30	3.47	-0.27
SARC	248.2	-118.0	83.1	45.7	-59.0	-26.9	7.89	0.30	3.53	-0.29
Mean	243.6	-118.1	83.2	45.7	-58.4	-26.2	7.80	0.30	3.47	-0.28
STD	4.3	0.2	1.2	0.1	0.4	0.5	0.11	0.01	0.05	0.01
%STD	1.78%	-0.13%	1.39%	0.13%	-0.65%	-1.94%	1.38%	3.45%	1.38%	-3.27%

Note: STD = standard deviation

**Table 3 Summary of turbulence model effects for cold-air jet,  $Re = 25 \times 10^6$ ,  $PR = 130$** 

TM	$F_A$ (N)	$F_j$ (N)	$F_{ji}$ (N)	$M_{j(0)}$ (N-m)	$M_{ji(0)}$ (N-m)	$M_{ji}$ (N-m)	$X_{cp}/D$	$K_f$	$K_m$	$K_{m(0)}$
SST	397.9	-118.5	105.3	45.9	-74.1	-33.4	7.82	0.11	4.13	-0.62
BSL	405.5	-118.8	106.0	46.0	-73.2	-32.2	7.67	0.11	4.01	-0.59
kw	413.1	-118.4	103.0	45.8	-73.3	-33.5	7.91	0.13	4.14	-0.60
rkw	417.8	-118.6	102.8	45.9	-73.2	-33.4	7.91	0.13	4.13	-0.60
rke	411.8	-118.6	101.7	45.9	-70.9	-31.5	7.75	0.14	3.95	-0.54
cke	409.3	-118.6	103.1	45.9	-72.1	-32.2	7.77	0.13	4.02	-0.57
keR	417.6	-118.6	101.0	45.9	-71.5	-32.4	7.87	0.15	4.04	-0.56
SA	419.2	-118.5	101.7	45.9	-71.9	-32.6	7.86	0.14	4.05	-0.57
SARC	421.2	-118.5	104.3	45.9	-74.0	-33.6	7.88	0.12	4.15	-0.61
Mean	412.6	-118.6	103.2	45.9	-72.7	-32.8	7.83	0.13	4.07	-0.58
STD	7.5	0.1	1.7	0.0	1.1	0.7	0.08	0.01	0.07	0.02
%STD	1.81%	-0.09%	1.64%	0.09%	-1.54%	-2.21%	1.03%	10.8%	1.71%	-4.23%

The force amplification factors for  $PR = 130$  are about one-half of those for  $PR = 220$  due to the induced JI force being about 1.25 times higher for the lower  $PR$ . The density (and resulting dynamic pressure) of the crossflow is 1.7 times higher for the  $PR = 130$  case. In the previous cold-air study described in DeSpirito,<sup>15</sup> it was found that the JI force and moment increase with  $PR$  while keeping the crossflow properties constant and changing the jet total pressure. However, in the current study, the crossflow properties in the lower  $PR$  case amplify the JI force and moment, even though the higher dynamic pressure leads to a slightly smaller barrel shock. The experimental setup from the earlier study<sup>5-10,15</sup> allowed the crossflow properties to be kept constant while changing the jet total conditions. However, in the experimental setup of the present study<sup>11,12</sup> the jet total conditions are determined from the solid propellant charge. Thus, it was likely easier to change  $PR$  by changing the crossflow conditions of the wind tunnel.

For the cold-air configuration at both Reynolds numbers, the standard deviations of all relevant forces, moments, and amplification factors were less than 5%. One exception was  $K_f$  at  $PR = 130$ , which was nearly 11%, but is still reasonable considering the small value of  $K_f$  at this  $PR$ . These results are similar to those obtained in the earlier study of cold-air jets in the DLR CCF missile configuration described in DeSpirito.<sup>15</sup>

From these cold-air results, one can conclude that the resulting aerodynamic forces and moments on the missile are fairly insensitive to the pressure differences arising from the various turbulence models. While this is a good result for this validation

case, one should use a “cold” jet only if that is indeed the temperature of the jet being simulated. It will be shown in Sections 3.2 and 3.3 that a cold-air jet provides the least accurate prediction of the surface pressure profiles resulting from a multispecies hot-gas jet interaction.

### 3.2 Hot-Gas Jet

---

For the multispecies hot-gas jet, the SST model was found to give the best overall results, and these are shown in Figs. 9 and 10 along with the results of Hold et al.<sup>14</sup> for comparison. For both *PRs*, the forward separation location and extent are predicted reasonably well. However, the pressure recovery in the region behind the jet is not predicted as accurately as in the cold-air jet cases. The CFD predicts an overshoot (similar to the cold-air CFD and experimental data) as the pressure recovers from the low pressures induced by the under-expanded jet, while the experiment shows a gradual pressure rise during this process with little or no overshoot. This would indicate an absence of the recompression shock impacting the missile surface in the experiment. Hold et al.’s predictions of the hot-gas jet surface pressures compared very well to the experimental data, including the absence of pressure recovery overshoot. A possible reason for the lack of pressure recovery overshoot in the experimental data could be the presence of some secondary combustion of unburned propellant that may have been ejected from the nozzle, which would modify the JI flowfield. However, Hold et al.’s predictions, like those in the present study, did not include reacting species yet still more closely predicted the pressure recovery. Some differences are observed between the predicted and experimental pressure profiles for the  $\phi \neq 180^\circ$  locations, but the comparisons are still generally reasonable.

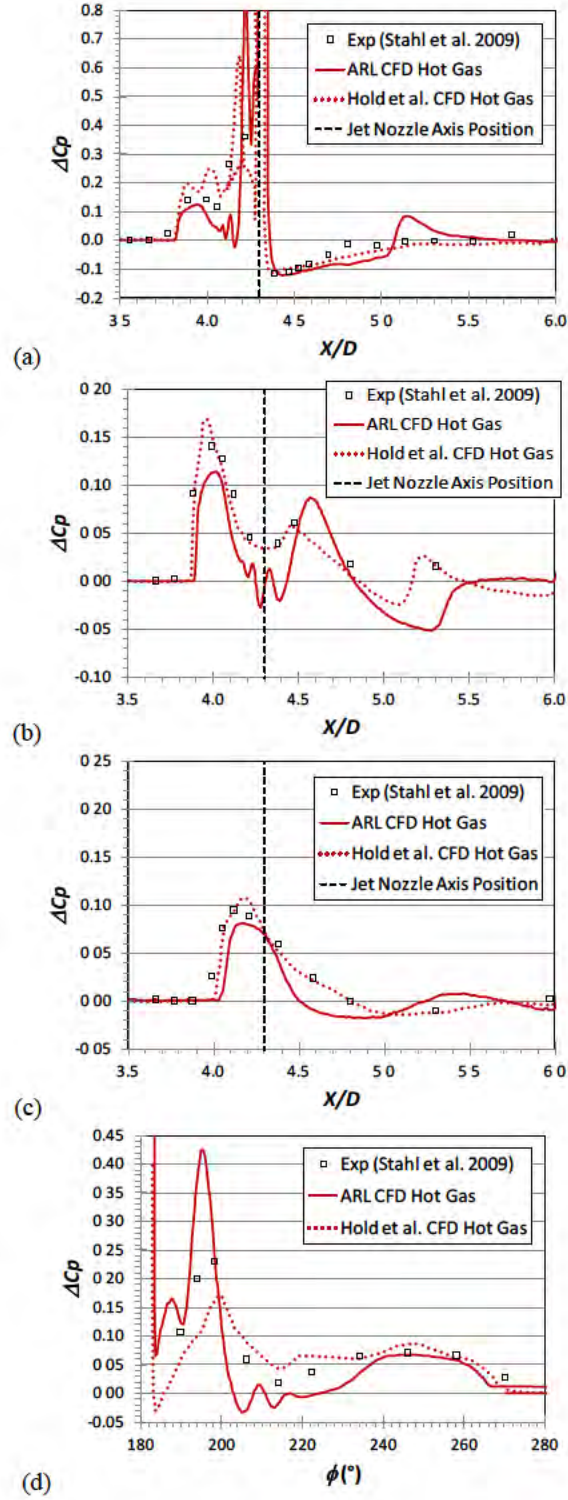


**Fig. 9** Hot-gas jet surface pressure profiles longitudinally along missile axis at (a)  $\phi = 180^\circ$ , (b)  $\phi = 150^\circ$ , (c)  $\phi = 120^\circ$ , and (d) circumferentially at  $X/D = 4.3$ , SST turbulence model,  $Re = 14 \times 10^6$ ,  $PR = 220$

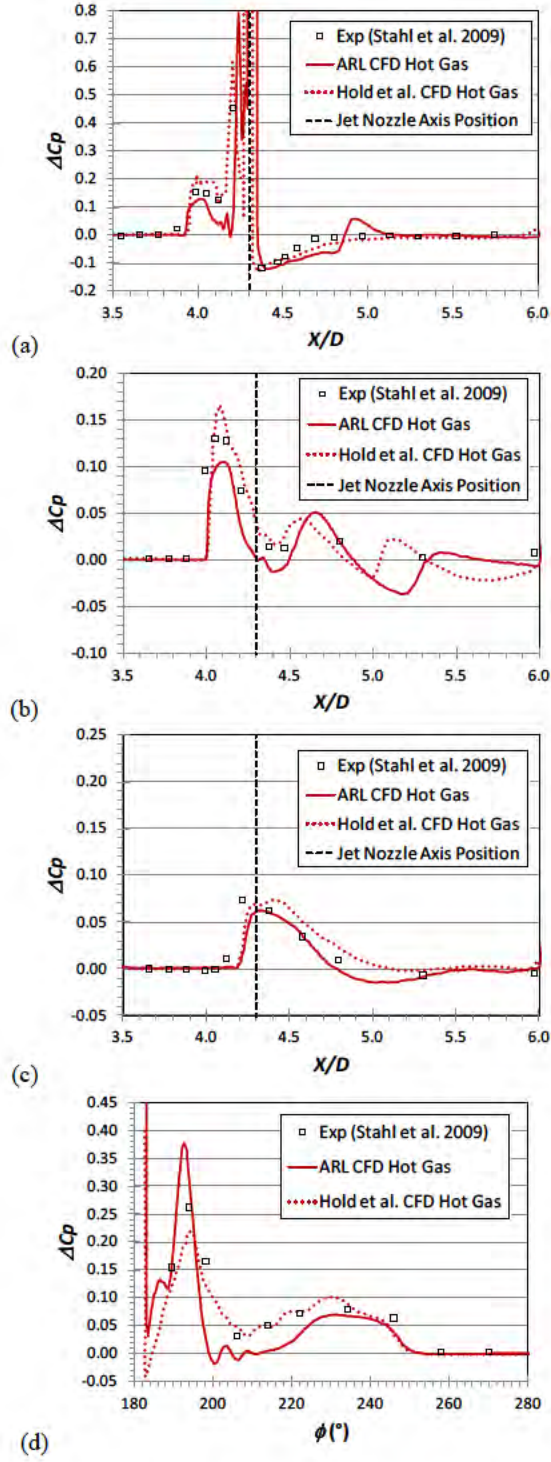


**Fig. 10** Hot-gas jet surface pressure profiles longitudinally along missile axis at (a)  $\phi = 180^\circ$ , (b)  $\phi = 150^\circ$ , (c)  $\phi = 120^\circ$ , and (d) circumferentially at  $X/D = 4.3$ , SST turbulence model,  $Re = 25 \times 10^6$ ,  $PR = 130$

Figures 11–13 show the comparison of the SST with the other 8 turbulence models for the  $PR = 220$  case. The SST model provides the best prediction of the forward separation location and extent when compared with all the other turbulence models, which again is important in predicting the pressure profiles for the  $\phi \neq 180^\circ$  locations. All turbulence models predict the overshoot in the pressure recovery region rather than the gradual rise of the experimental data. For the  $PR = 220$  results, the rkw, rke, and cke come closest to the SST model predictions (Fig. 12). Appendix B shows the  $PR = 130$  results, where the SST model is again the only one to accurately predict the forward separation location and extent. In this case, the rkw, rke, and cke are again the next closest to the experimental data at  $\phi = 180^\circ$ , but the predictions are slightly poorer than those at  $PR = 220$ . For both  $PR$  the variation in predicted pressure among turbulence models is generally less in the region behind the jet at the  $\phi = 180^\circ$  location and circumferentially to the side of the jet, up to about  $\phi = 200^\circ$ . This indicates that the predictions of the jet near-field flow structures in these directions are insensitive to the turbulence model. Beyond  $\phi = 200^\circ$  circumferentially, the differences in the forward separation prediction begin to impact the circumferential pressure profiles.



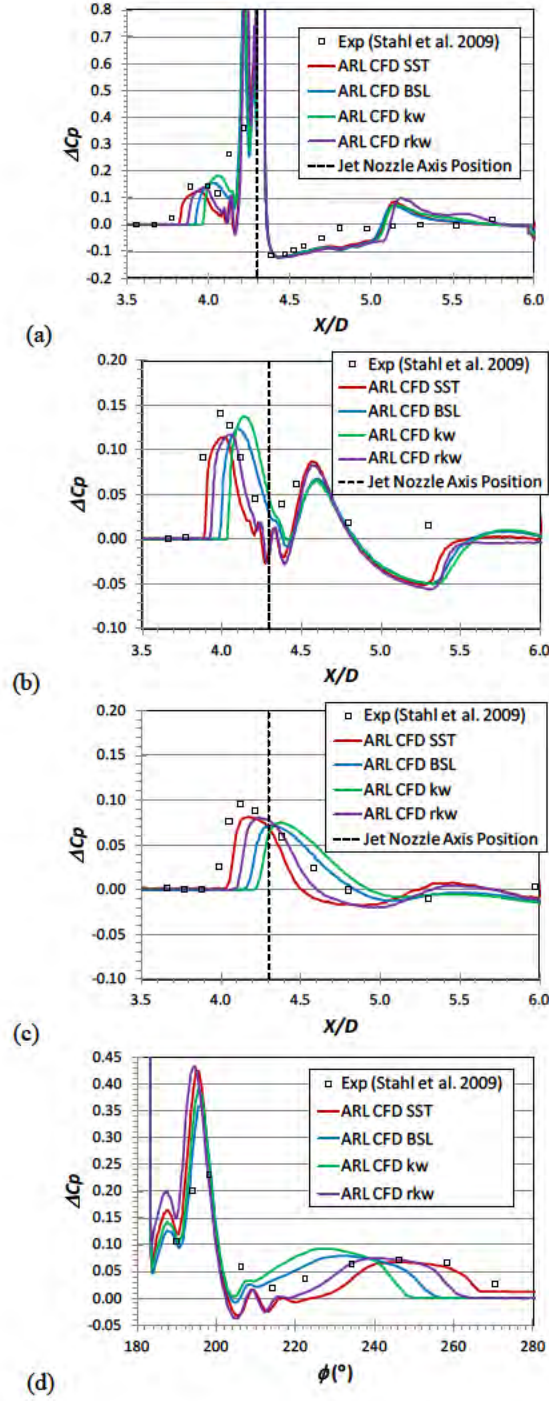


**Fig. 11** Effect of  $k-\omega$ -based turbulence models on hot-gas jet surface pressure profiles longitudinally along missile axis at (a)  $\phi = 180^{\circ}$ , (b)  $\phi = 150^{\circ}$ , (c)  $\phi = 120^{\circ}$ , and (d) circumferentially at  $X/D = 4.3$ ,  $Re = 14 \times 10^6$ ,  $PR = 220$



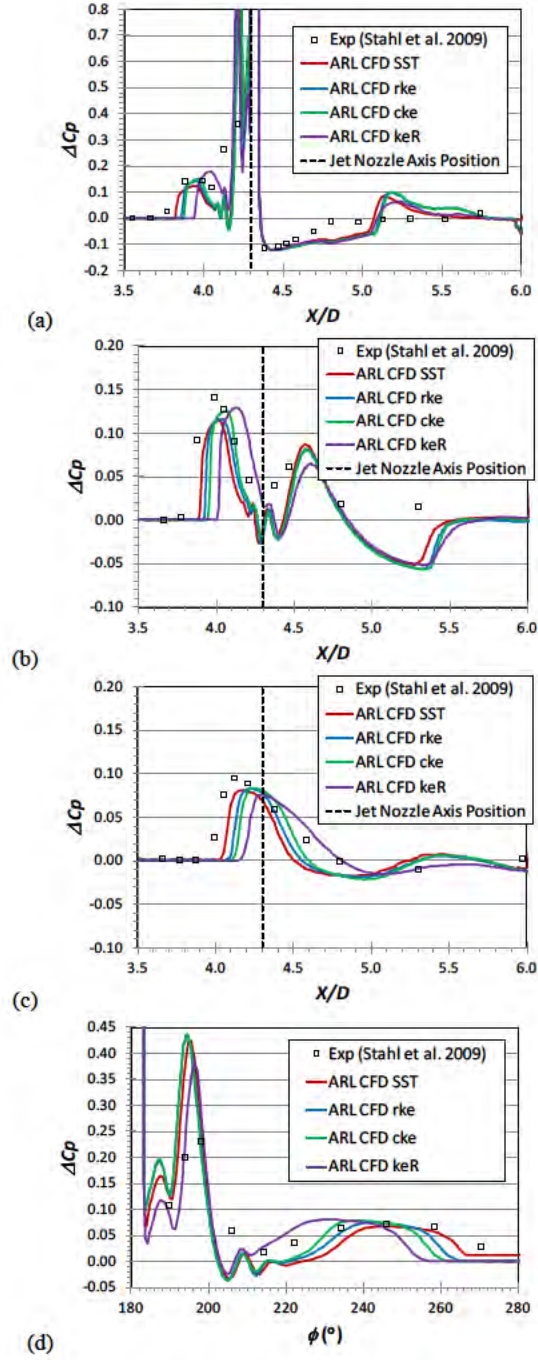


**Fig. 12 Effect of SST and  $k$ - $\varepsilon$ -based turbulence models on hot-gas jet surface pressure profiles longitudinally along missile axis at (a)  $\phi = 180^\circ$ , (b)  $\phi = 150^\circ$ , (c)  $\phi = 120^\circ$ , and (d) circumferentially at  $X/D = 4.3$ ,  $Re = 14 \times 10^6$ ,  $PR = 220$**

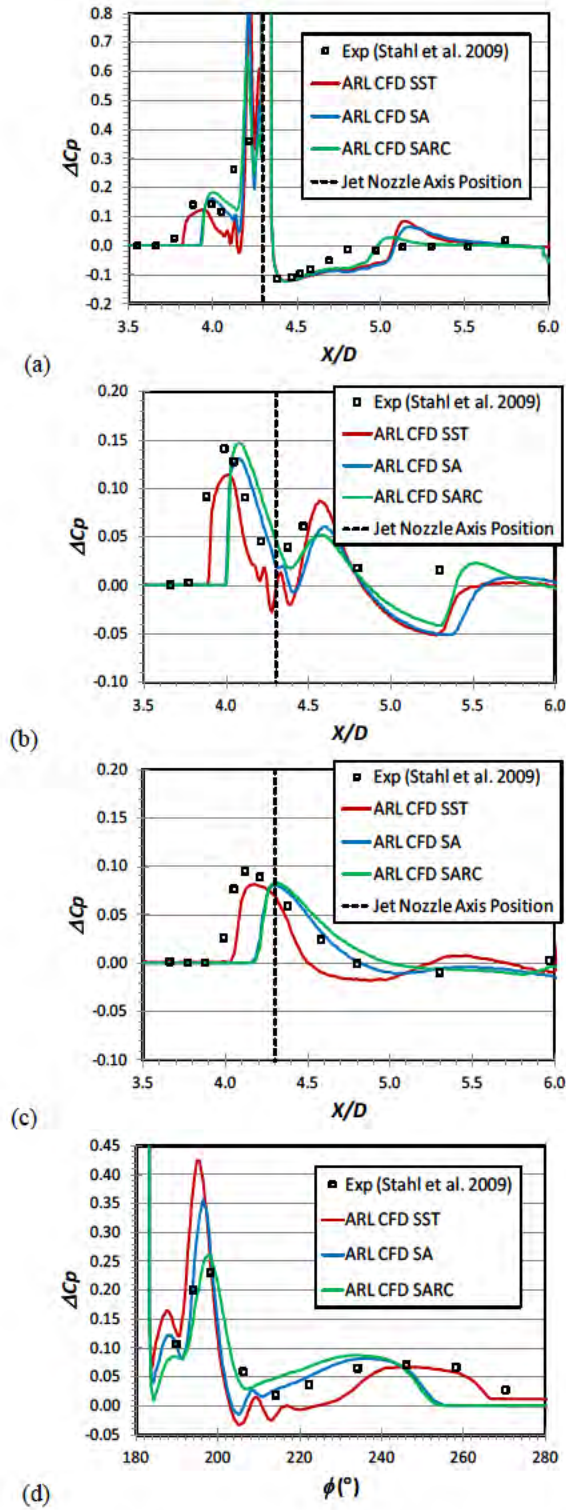


**Fig. 13** Effect of SST and SA-based turbulence models on hot-gas jet surface pressure profiles longitudinally along missile axis at (a)  $\phi = 180^\circ$ , (b)  $\phi = 150^\circ$ , (c)  $\phi = 120^\circ$ , and (d) circumferentially at  $X/D = 4.3$ ,  $Re = 14 \times 10^6$ ,  $PR = 220$

Tables 4 and 5 show the summary comparison of turbulence model results for the hot-gas,  $PR = 220$  and  $130$  cases, respectively. The variation of the aerodynamic forces and moments is  $\leq 13\%$ , with the JI force and moment showing the largest variation, as might be expected. This level of variation is not unreasonable, considering the complexity of the problem. The amplification factors show much larger variation, but this is mostly due to the small magnitude of the amplification factors. For example, the JI force magnitude is nearly 90% of the jet thrust force magnitude in the  $PR = 130$  case (Table 5), which causes the force amplification factor to approach zero (Eq. 1). The mean values of the JI force and moment and their amplification factors are similar to those observed in the cold-air results. However, the increased variability of the JI force and moment in the hot-gas case (approximately 10% vs. 1% for cold-air case) is accentuated in the calculation of amplification factor as it approaches zero.

**Table 4 Summary of turbulence model effects for hot-gas jet,  $Re = 14 \times 10^6$ ,  $PR = 220$**

TM	$F_A$ N	$F_j$ N	$F_{ji}$ N	$M_{j(0)}$ N-m	$M_{ji(0)}$ N-m	$M_{ji}$ N-m	$X_{cp}/D$	$K_f$	$K_m$	$K_{m(0)}$
SST	238.9	-116.0	77.9	44.9	-60.4	-30.3	8.63	0.33	3.90	-0.35
BSL	235.6	-116.1	74.4	44.9	-59.8	-31.0	8.93	0.36	3.96	-0.33
kw	245.4	-116.1	67.4	44.9	-55.2	-29.1	9.10	0.42	3.79	-0.23
rkW	243.0	-116.2	69.2	45.0	-53.8	-27.0	8.63	0.40	3.58	-0.20
rke	243.1	-115.6	70.6	44.7	-54.7	-27.4	8.61	0.39	3.63	-0.22
cke	241.5	-116.5	72.0	45.1	-55.8	-28.0	8.62	0.38	3.67	-0.24
keR	248.3	-115.3	66.8	44.6	-51.7	-25.8	8.60	0.42	3.49	-0.16
SA	248.5	-115.8	68.5	44.8	-54.2	-27.7	8.79	0.41	3.66	-0.21
SARC	247.0	-115.8	86.7	44.8	-71.9	-38.3	9.21	0.25	4.68	-0.60
Mean	243.5	-115.9	72.6	44.9	-57.5	-29.4	8.79	0.37	3.82	-0.28
STD	4.4	0.3	6.4	0.1	6.1	3.7	0.24	0.05	0.36	0.14
%STD	1.79%	-0.29%	8.75%	0.29%	-10.6%	-12.7%	2.7%	14.6%	9.36%	-48.1%

**Table 5 Summary of turbulence model effects for hot-gas jet,  $Re = 25 \times 10^6$ ,  $PR = 130$** 

TM	$F_A$ N	$F_j$ N	$F_{ji}$ N	$M_{j(0)}$ N-m	$M_{ji(0)}$ N-m	$M_{ji}$ N-m	$X_{cp}/D$	$K_f$	$K_m$	$K_{m(0)}$
SST	404.7	-116.1	111.6	44.9	-87.6	-44.4	8.72	0.04	5.25	-0.95
BSL	397.4	-116.2	105.6	45.0	-85.4	-44.5	8.98	0.09	5.26	-0.90
kw	413.8	-116.2	98.8	44.9	-81.4	-43.1	9.15	0.15	5.13	-0.81
rkw	418.6	-116.0	99.3	44.9	-81.8	-43.4	9.15	0.14	5.15	-0.82
rke	409.8	-115.8	97.5	44.8	-76.8	-39.1	8.76	0.16	4.75	-0.71
cke	406.0	-115.9	98.8	44.8	-77.0	-38.8	8.66	0.15	4.72	-0.72
keR	415.6	-116.2	86.3	45.0	-68.6	-35.2	8.83	0.26	4.37	-0.53
SA	418.0	-116.0	89.3	44.9	-72.3	-37.8	9.00	0.23	4.62	-0.61
SARC	415.2	-116.1	118.7	44.9	-97.4	-51.4	9.11	-0.02	5.92	-1.17
Mean	411.0	-116.1	100.7	44.9	-80.9	-42.0	8.9	0.13	5.0	-0.8
STD	7.1	0.2	10.2	0.1	8.6	4.8	0.19	0.09	0.46	0.19
%STD	1.73%	-0.13%	10.1%	0.13%	-10.7%	-11.5%	2.14%	65.9%	9.21%	-23.9%

### 3.3 Hot-Air Jet

A third case investigated here and by Hold et al.<sup>14</sup> was that of an ideal-gas (air) jet at the temperature of the solid propellant combustion products. This is the most likely scenario to use if one does not wish to use a real-gas solution with multispecies products. Figures 14–15 compare the multispecies, hot-gas experimental pressures and predicted pressures for the multispecies hot-gas jet, ideal-gas hot-air jet, and the ideal-gas cold-air jet cases. The predictions are all from simulations using the SST turbulence model. Although the BSL model more closely predicted the cold-air experimental data, the hot-air jet predictions with the SST model, like those for the hot-gas jet, compared best with the hot-gas experimental data. For both  $PR$ s, the hot-gas jet predictions are the most accurate, as expected, but the hot-air predictions are reasonable. In fact, the variation among the 3 predictions in the forward separation region is within the range observed for the variation among turbulence models. There is more sensitivity to the jet temperature and thermodynamic properties in the downstream interaction area, as indicated by the variation among the 3 jet cases, especially the location of the recovery pressure overshoot near  $X/D = 5$  on the  $\phi = 180^\circ$  profile.

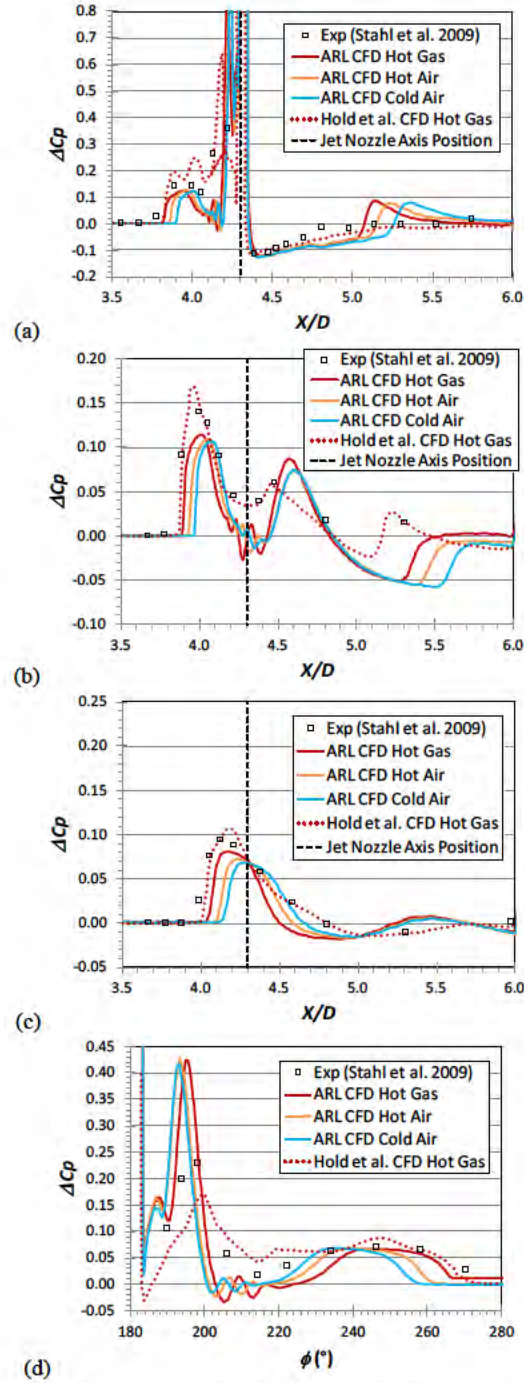


**Fig. 14** Surface pressure profiles longitudinally along missile axis at (a)  $\phi = 180^\circ$ , (b)  $\phi = 150^\circ$ , (c)  $\phi = 120^\circ$ , and (d) circumferentially at  $X/D = 4.3$ , SST turbulence model,  $Re = 14 \times 10^6$ ,  $PR = 220$



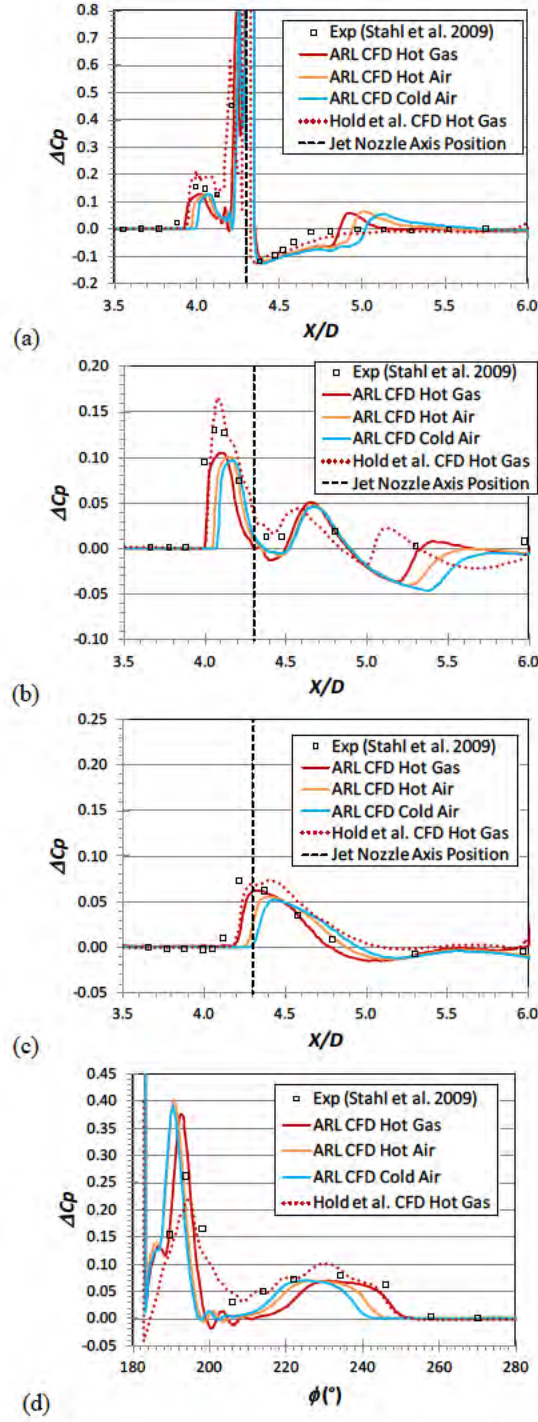


**Fig. 15** Surface pressure profiles longitudinally along missile axis at (a)  $\phi = 180^\circ$ , (b)  $\phi = 150^\circ$ , (c)  $\phi = 120^\circ$ , and (d) circumferentially at  $X/D = 4.3$ , SST turbulence model,  $Re = 25 \times 10^6$ ,  $PR = 130$

The JI flowfield is likely more sensitive to the flow density in the jet wake flow than to the varying thermodynamic properties of the jet (though the latter obviously has some effect). For instance, probing the wake at  $X/D = 5.2$ ,  $Z/D = 0.65$ ,  $\phi = 180^\circ$

for each of the 3 cases in Fig. 14 showed densities of 0.36, 0.39, and 0.89 kg/m<sup>3</sup> for the hot-gas, hot-air, and cold-air cases, respectively. The corresponding temperatures were 362, 278, and 144 K, but the static pressure only varied by 18%, from 37.9 for the hot-gas jet down to 31.2 kPa for the cold-air jet. The largest differences in the JI flowfield occur between the cold-air and hot-air cases rather than between ideal- and real-gas effects of varying thermodynamic properties (hot-air and hot-gas cases); this difference manifests itself in the surface pressure profiles.

Tables 6 and 7 show the summary comparison of turbulence model results for the hot-air,  $PR = 220$  and 130 cases, respectively. The variation of the aerodynamic forces and moments is less than 10% and generally the results are comparable to the hot-gas results (Tables 4 and 5). In fact, the maximum difference between the hot-gas and hot-air jet JI forces and moments are 4.8% and 10%, respectively, which are within their variation with turbulence model. These results indicate that the ideal-gas, hot-air jet may provide adequate predictions of the aerodynamic forces and moments and a multispecies real-gas solution may not be required. A similar conclusion was made by Hold et al.<sup>14</sup> Of course, if one believes that secondary combustion in the JI region is very likely, a reacting, multispecies real-gas solution should be investigated.

**Table 6 Summary of turbulence model effects for hot-air jet,  $Re = 14 \times 10^6$ ,  $PR = 220$**

TM	$F_A$ (N)	$F_j$ (N)	$F_{ji}$ (N)	$M_{j(0)}$ (N-m)	$M_{ji(0)}$ (N-m)	$M_{ji}$ (N-m)	$X_{cp}/D$	$K_f$	$K_m$	$K_{m(0)}$
SST	236.5	-117.4	75.8	45.4	-58.0	-28.7	8.51	0.35	3.71	-0.28
BSL	240.4	-117.3	78.6	45.4	-58.4	-27.9	8.25	0.33	3.65	-0.29
kw	246.0	-117.3	71.7	45.4	-55.9	-28.1	8.65	0.39	3.66	-0.23
rkW	249.0	-117.2	71.4	45.3	-55.6	-28.0	8.65	0.39	3.65	-0.23
rke	244.6	-116.8	73.7	45.2	-55.4	-26.9	8.36	0.37	3.56	-0.23
cke	242.2	-116.9	75.7	45.2	-56.6	-27.3	8.31	0.35	3.60	-0.25
keR	248.2	-116.7	68.4	45.1	-51.7	-25.3	8.40	0.41	3.41	-0.15
SA	249.1	-117.0	70.8	45.3	-53.6	-26.2	8.41	0.40	3.49	-0.18
SARC	249.2	-117.1	84.1	45.3	-66.0	-33.5	8.73	0.28	4.18	-0.46
Mean	245.0	-117.1	74.5	45.3	-56.8	-28.0	8.47	0.36	3.66	-0.25
STD	4.5	0.3	4.7	0.1	4.0	2.3	0.17	0.04	0.22	0.09
%STD	1.85%	-0.23%	6.36%	0.23%	-7.08%	-8.32%	2.01%	11.0%	5.99%	-34.7%

**Table 7 Summary of turbulence model effects for hot-air jet,  $Re = 25 \times 10^6$ ,  $PR = 130$** 

TM	$F_A$ (N)	$F_j$ (N)	$F_{ji}$ (N)	$M_{j(0)}$ (N-m)	$M_{ji(0)}$ (N-m)	$M_{ji}$ (N-m)	$X_{cp}/D$	$K_f$	$K_m$	$K_{m(0)}$
SST	397.6	-117.7	105.9	45.6	-81.3	-40.3	8.53	0.10	4.80	-0.78
BSL	405.1	-117.6	108.2	45.5	-81.2	-39.4	8.34	0.08	4.72	-0.78
kw	413.2	-117.7	100.4	45.5	-77.9	-39.1	8.62	0.15	4.69	-0.71
rkw	417.9	-117.5	100.6	45.5	-78.2	-39.2	8.63	0.14	4.71	-0.72
rke	412.8	-117.2	93.8	45.3	-69.8	-33.5	8.27	0.20	4.18	-0.54
cke	410.2	-117.2	95.5	45.4	-71.4	-34.4	8.30	0.18	4.26	-0.57
keR	419.1	-117.0	91.8	45.3	-69.8	-34.3	8.45	0.21	4.26	-0.54
SA	420.1	-117.3	94.5	45.4	-72.3	-35.7	8.50	0.19	4.38	-0.59
SARC	420.1	-117.4	113.9	45.4	-88.6	-44.6	8.65	0.03	5.22	-0.95
Mean	412.9	-117.4	100.5	45.4	-76.7	-37.8	8.48	0.14	4.58	-0.69
STD	7.7	0.3	7.5	0.1	6.4	3.6	0.15	0.06	0.34	0.14
%STD	1.86%	-0.22%	7.46%	0.22%	-8.37%	-9.55%	1.72%	43.6%	7.36%	-20.2%

Figure 16 shows flowfield Mach contours, surface pressure contours, and simulated surface oil flow streamlines for the 3 cases using the SST turbulence model and  $PR = 220$ . The flow characteristics are very similar, although the pressure profiles features shown in Fig. 14a can be observed. First, the forward separation location is farthest forward for the hot-gas jet case and nearest the jet nozzle in the cold-air case. Perhaps harder to observe in Fig. 16 is that the location of the pressure overshoot point (end of dark-blue  $C_p$  contour) is nearest the jet nozzle exit for the hot-gas jet case and farthest for the cold-air case. In all 3 cases, the recompression shock emanates from the shock interactions behind the barrel shock Mach disk and impacts the missile surface near the end of the dark-blue low-pressure region.

The lack of the pressure recovery overshoot in the experimental hot-gas data indicates a much weaker shock or no shock at this location. As stated earlier, this could be explained by some secondary combustion of expelled solid propellant in the experimental hot-gas jet gases. Hold et al.'s<sup>14</sup> hot-gas predictions did not show this pressure recovery overshoot either, but his flowfield (see Fig. 6) fairly closely resembles that in Fig. 16e. Unfortunately, Hold et al.<sup>15</sup> did not include any surface pressure contours to compare. Hold et al.'s predictions of the hot-air case (not shown here) did include the pressure overshoot, as in the present predictions.



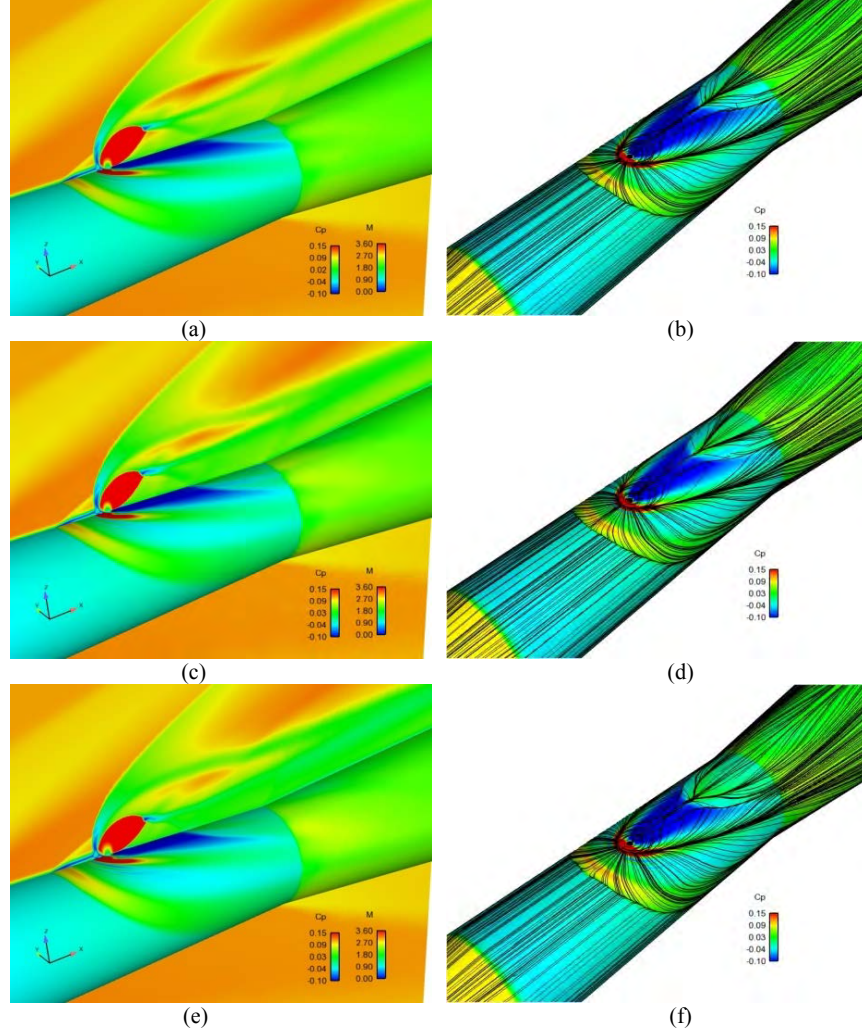


**Fig. 16** Mach contours on symmetry plane and  $C_p$  contours on missile surface (a, c, e) and simulated surface oil flow streamlines and  $C_p$  contours on missile surface (b, d, f) for (a, b) cold-air, (c, d) hot-air, and (e, f) hot-gas jets; SST turbulence model,  $Re = 14 \times 10^6$ ,  $PR = 220$

### 3.4 Comment on Turbulence Models

This study has investigated several popular turbulence models in use today for their performance in predicting both a single- and multispecies, supersonic jet in a supersonic crossflow. It is difficult to provide definitive reasons for one model performing better over another, as these jet-in-crossflow problems are very difficult for RANS models to accurately predict on a consistent basis. The flows present in this problem include shock-boundary-layer interactions, boundary-layer separation and reattachment, and rotating flows. One might expect the SST model to perform well, as it was designed to improve prediction of adverse pressure gradient flow, including more accurate prediction of separation and reattachment.<sup>18</sup> Indeed, it has

performed reasonably well in this study (hot-air and hot-gas cases), in the study of Hold et al.<sup>14</sup> and previously in the study of Gnemmi and Schafer.<sup>6</sup> The BSL model also performed well in the cold-air simulations of this study and a previous one using cold-air.<sup>15</sup> Menter's BSL and SST models are very similar, the primary difference being the accounting for the effect of the transport of the principle turbulent shear stress in the SST model.<sup>18</sup> Both the BSL and SST models use the  $k-\omega$  model in the inner region of the boundary layer and switch to the  $k-\varepsilon$  model in the outer region and in free shear flows. This helps these models avoid the original  $k-\omega$  model's strong sensitivity to freestream  $\omega$  values and less accurate modeling of the wake region of the boundary layer. The only nonlinear model investigated, the cke model, did not outperform the SST or BSL models. The compressibility correction<sup>26,27</sup> was also used in all these simulations, as the Mach number in the under-expanded jet flowfield is very high and was shown to improve results in the previous study on this configuration.<sup>15</sup>

Similar limitations on the accuracy of RANS turbulence models to predict shock wave/turbulent boundary-layer interactions have been reported by Georgiadis et al.,<sup>28,29</sup> Hirsh,<sup>30</sup> and DeBonis.<sup>31</sup> As Dash et al.<sup>27</sup> and Georgiadis et al.<sup>28</sup> state, RANS models are still the primary choice in practical, applied CFD such as that used for early design development, system performance assessment, and design optimization studies and, as such, are in need of continued development. The user must be aware of the limitations of these models to make valid conclusions on the accuracy of the results.

This report's author usually uses the SST model for jet-in-crossflow and shock-boundary-layer problems. Although a study of the number of turbulence models performed in the present study cannot feasibly be done routinely, it is suggested to at least try 2 or 3 of the turbulence models available in your solver that are appropriate for the flow of interest. Also note what modifications to the standard turbulence models may be available in your solver. For instance, although it was not used in this study, CFD<sup>++</sup> has available a modification to the realizable  $k-\varepsilon$  model with a turbulence production limiter applied to the  $k$ -equation.<sup>17</sup> This allows better prediction of higher-fidelity flow-separation bubbles, similar to the SST model.

## 4. Summary and Conclusions

---

CFD simulations of surface pressures resulting from lateral jet injection into a Mach 3 supersonic crossflow from a cone-cylinder-flare missile were presented. Simulations were completed for an ideal-gas cold-air jet, a nonreacting multispecies hot-gas jet, and an ideal-gas hot-air jet. Predictions of the longitudinal and azimuthal pressure profiles along the missile body were very good to excellent when using the best-performing turbulence model for each case. However, the extent of the rear separation region was over predicted in the hot-gas jet cases.

A total of 9 turbulence models were compared with the intent to estimate the level of variation in the predicted results. Menter's BSL turbulence model was found to give the best results for the cold-air cases, while Menter's SST turbulence model was found to give the best results for the hot-gas jet and hot-air jet cases. The surface pressure profiles showed significant variation with turbulence model, but the resulting aerodynamic forces and moments were fairly insensitive to the pressure differences arising from the various turbulence models. The variation of forces and moments with turbulence model was less than 13% for the hot-gas jet cases and less than 3% for the cold-air jet cases. These trends held for both pressure ratios and Reynolds numbers investigated.

The ideal-gas hot-air jet compared reasonably well to the hot-gas jet, with the variation of aerodynamic forces and moments with turbulence model less than 10%. Therefore, it is reasonable to use the hot-air jet if one does not wish to use a real-gas multispecies simulation. However, one must be aware that any secondary combustion in the external flowfield would make using a reacting-gas simulation more important.

Unfortunately, the lack of availability of experimental force and moment data prohibits the determination of the actual accuracy of the computational results. However, comparisons of ARL results with other cold-air and hot-gas CFD results from Hold et al.<sup>14</sup> and cold-air CFD results from ISL<sup>6,15</sup> showed very good agreement.

Similar variations in turbulence model performance have been found in other high-Mach-number flows, especially shock-boundary-layer interactions, by several researchers.

## 5. References and Notes

---

1. Mahesh, K. The interaction of jets with crossflow. *Annual Review of Fluid Mechanics*. 2013;45:379–407.
2. Margason RJ. Fifty years of jet in cross flow research: computational and experimental assessment of jets in cross flow. Moffett Field (CA): NASA Ames Research Center; 1993 Nov. Report No.: AGARD-CP-534.
3. DeSpirito J. Factors affecting reaction jet interaction effects on projectiles. Presented at the 29th AIAA Applied Aerodynamics Conference; 2011 Jun; Honolulu, HI.
4. DeSpirito J. Lateral jet interaction on a finned projectile in supersonic flow. Presented at the 50th AIAA Aerospace Sciences Meeting; 2012 Jan; Nashville, TN.
5. DeSpirito J. Lateral reaction jet flow interaction effects on a generic fin-stabilized munition in supersonic crossflows. Aberdeen Proving Ground (MD): Army Research Laboratory (US); 2013 Nov. Report No.: ARL-TR-6707. Also available at: <http://www.arl.army.mil/arlreports/2013/ARL-TR-6707.pdf>.
6. Gnemmi P, Schafer HJ. Experimental and numerical investigations of a transverse jet interaction on a missile body. Presented at the 43rd AIAA Aerospace Sciences Meeting; 2005 Jan; Reno, NV.
7. Gnemmi P, Adeli R, Longo J. Computational comparisons of the interaction of a lateral jet on a supersonic generic missile. Presented at the AIAA Atmospheric Flight Mechanics Conference; 2008 Aug; Honolulu, HI.
8. Gnemmi P, Eichhorn A, Emunds H, Esch H, Gulhan A, Leopold F, Schafer HJ. Experimental and computational study of the interaction between a lateral jet and the supersonic external flow on a generic missile body. Saint-Louis (France): Institute of Saint-Louis; 2006 May. PU 622/2006.
9. Stahl B, Esch H, Gulhan A. Experimental investigation of side jet interaction with a supersonic cross flow. *Aerospace Science and Technology*. 2008;2:269–275.
10. Adeli R, Longo JMA, Emunds H. Flow fields study of a supersonic jet exiting into a supersonic stream. In: *Notes on numerical fluid mechanics and multidisciplinary design*. Berlin (Germany): Springer; 2006. p. 160–167.

11. Stahl B, Emunds H, Gulhan A. Experimental investigation of hot and cold side jet interaction with a supersonic cross-flow. *Aerospace Science and Technology*. 2009;13:488–496.
12. Stahl B, Siebe F, Gulhan A. Hot-gas side jet in a supersonic freestream. *AIAA Journal of Spacecraft and Rockets*. 2010;47(6):957–965.
13. Sourgen F, Gauthier T, Leopold F, Sauerwein B. Substitution of hot-gas lateral jets by cold-gas jets in supersonic flows. *AIAA Journal of Spacecraft and Rockets*. 2011;48(1):81–92.
14. Hold RK, Engert M, Weinand K, Stern D. Numerical investigation of hot and cold side jet interaction with a supersonic cross-flow. In: *Notes on numerical fluid mechanics and multidisciplinary design*. Berlin (Germany): Springer-Verlag; 2013. p. 575–582.
15. DeSpirito J. Turbulence model effects on cold-gas lateral jet interaction in a supersonic crossflow. Aberdeen Proving Ground (MD): Army Research Laboratory (US); 2014 June. Report No.: ARL-TR-6964. Also available at: <http://www.arl.army.mil/arlreports/2014/ARL-TR-6964.pdf>.
16. MIME user manual. Agoura Hills (CA): Metacomp Technologies, Inc.; 2008.
17. CFD ++ User Manual. Agoura Hills (CA): Metacomp Technologies, Inc.; 2013.
18. Menter FR. Two-equation eddy-viscosity turbulence models for engineering applications. *AIAA Journal*. 1994;32(8):1598–1605.
19. Wilcox DC. Formulation of the k-omega turbulence model revisited. *AIAA Journal*. 2008;46(11):2823–2838.
20. Spalart PR, Allmaras SR. A One-equation turbulence for aerodynamic flows. *Recherche Aerospaciale*. 1994;1:5–21.
21. Shur ML, Strelets MK, Travin AK, Spalart PR. Turbulence modeling in rotating and curved channels: assessing the Spalart-Shur correction. *AIAA Journal*. 2000;38(5):784–792.
22. Chien KY. Predictions of channel and boundary layer flows with a low-Reynolds-number turbulence model. *AIAA Journal*. 1982;20(1):33–38.
23. Goldberg U, Batten P, Palaniswamy S, Chakravarthy S, Perroomian O. Hypersonic flow predictions using linear and nonlinear turbulence closures. *AIAA Journal of Aircraft*. 2000;37(4):671–675.

24. Goldberg U, Perroomian, O, Chakravarthy, S. Application of the  $k$ - $\epsilon$ -R turbulence model to wall-bounded compressive flows. Presented at the 36th AIAA Aerospace Sciences Meeting; 1998 Jan; Reno, NV.
25. DLR TAU code. [accessed 2014 Dec 3]. <http://tau.dlr.de/>.
26. Gross N, Blaisdell GA, Lyrintzis AS. Analysis of modified compressibility corrections for turbulence models. Presented at the 49th AIAA Aerospace Sciences Meeting; 2011 Jan; Orlando, FL.
27. Dash SM, Brinkman KW, Ott JD. Turbulence modeling advances and validation for high speed aeropropulsive flows. *International Journal of Aeroacoustics*. 2012;11(7,8):813–851.
28. Georgiadis NJ, Yoder DA, Vyas MA, Engblom WA. Status of turbulence modeling for hypersonic propulsive flowpaths. *Theoretical and Computational Fluid Dynamics*. 2014;28(3):295–318.
29. Georgiadis NJ, Rumsey CL, Huang GP. Revisiting turbulence model validation for high-Mach number axisymmetric compression corner flows. Presented at the 53rd Aerospace Sciences Meeting; 2015 Jan; Kissimmee, FL.
30. Hirsh, C. Lessons learned from the first AIAA SWBLI workshop: CFD simulations of two test cases. Presented at the 28th AIAA Applied Aerodynamics Conference; 2010 Jun; Chicago, IL.
31. DeBonis JR. Evaluation of industry standard turbulence models on an axisymmetric supersonic compression corner. Presented at the 53rd Aerospace Sciences Meeting; 2015 Jan; Kissimmee, FL.

## **Appendix A. Cold-Air Jet Turbulence Effects, $PR = 130$**

---

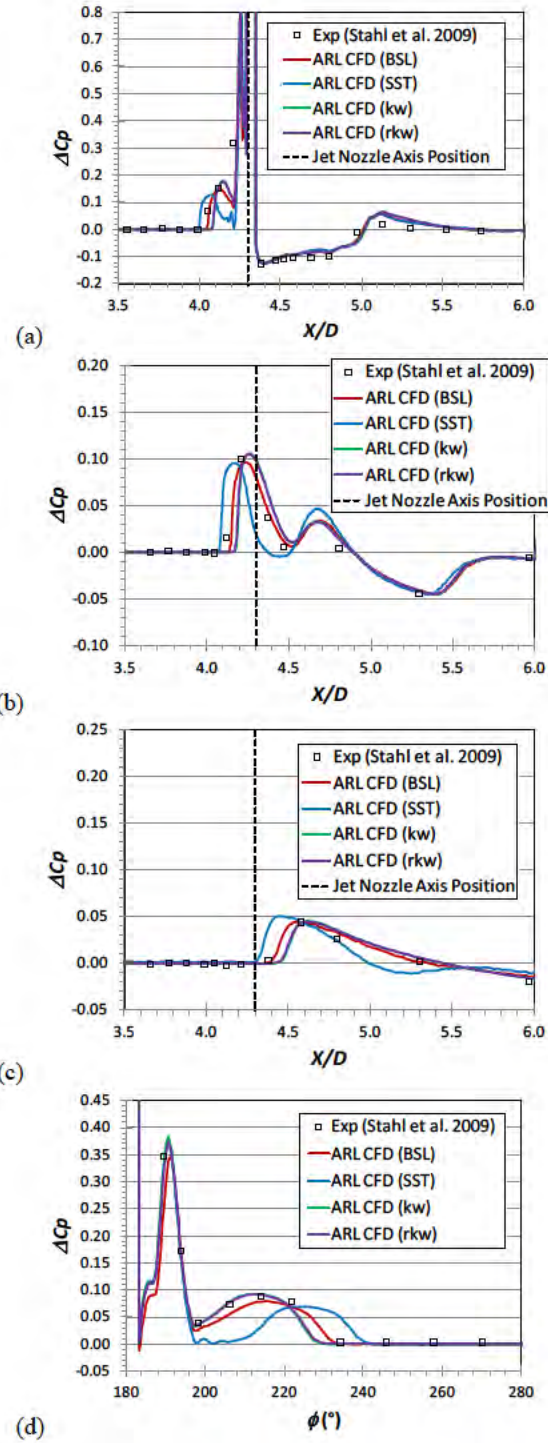


**Fig. A-1** Effect of  $k$ - $\omega$ -based turbulence models on cold-air jet surface pressure profiles longitudinally along missile axis at (a)  $\phi = 180^\circ$ , (b)  $\phi = 150^\circ$ , (c)  $\phi = 120^\circ$ , and (d) circumferentially at  $X/D = 4.3$ ,  $Re = 14 \times 10^6$ ,  $PR = 130$



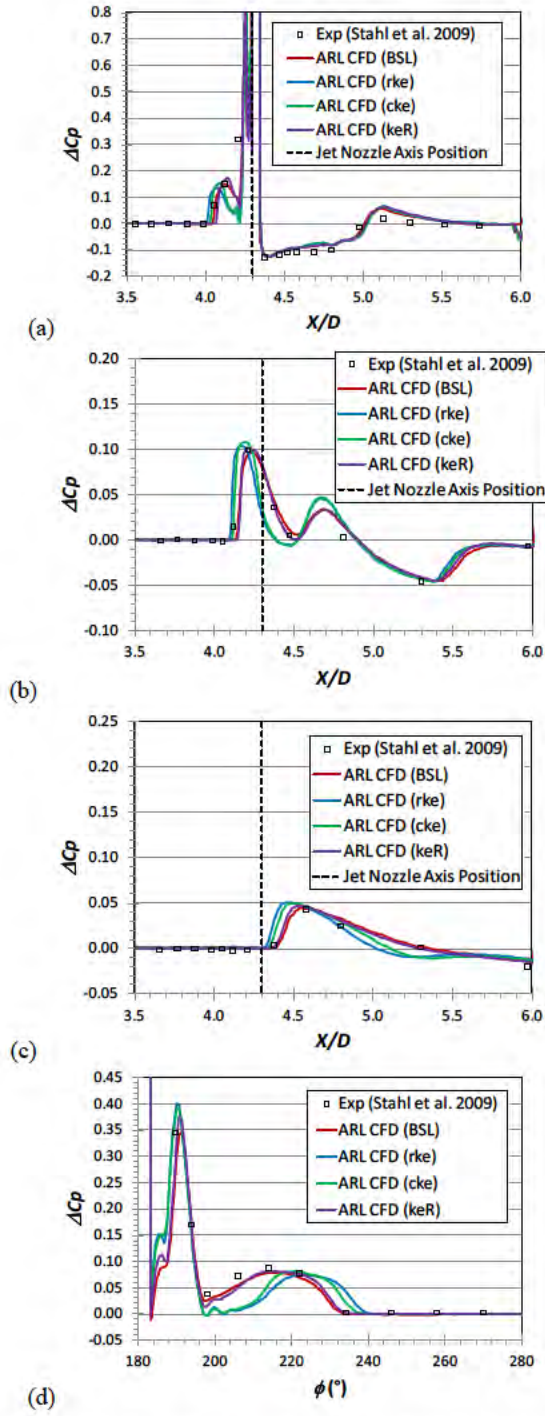


**Fig. A-2 Effect of Menter's baseline (BSL) and  $k-\varepsilon$ -based turbulence models on cold-air jet surface pressure profiles longitudinally along missile axis at (a)  $\phi = 180^\circ$ , (b)  $\phi = 150^\circ$ , (c)  $\phi = 120^\circ$ , and (d) circumferentially at  $X/D = 4.3$ ,  $Re = 14 \times 10^6$ ,  $PR = 130$**

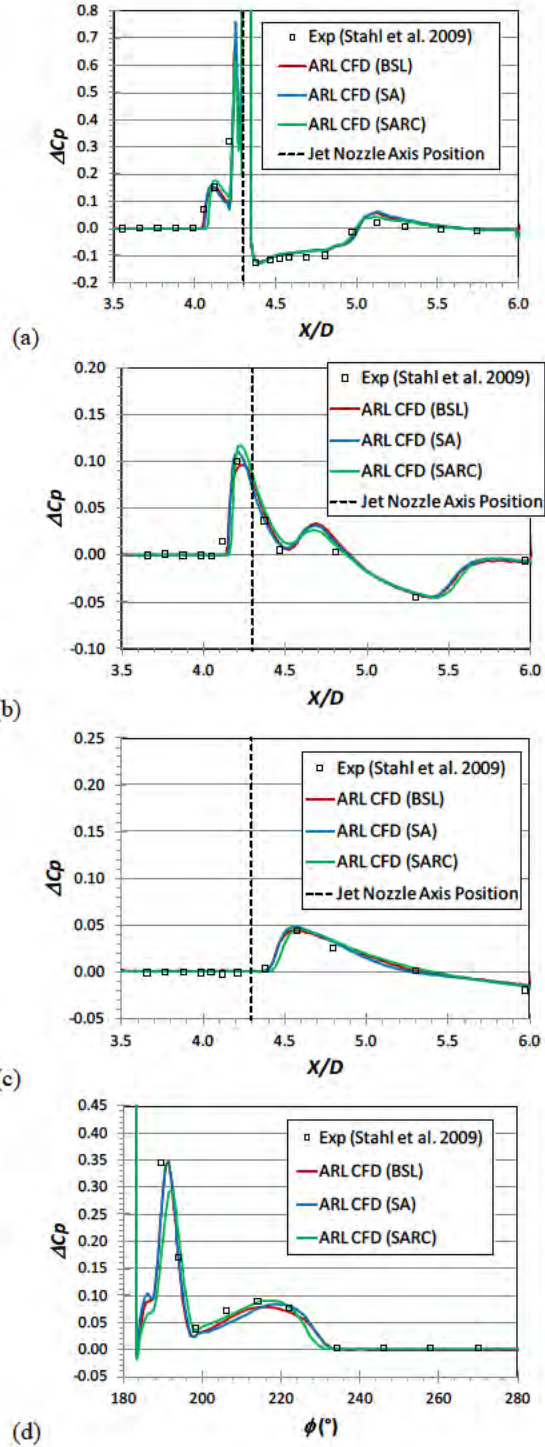


**Fig. A-3 Effect of BSL and Spalart-Allmaras-based turbulence models on cold-air jet surface pressure profiles longitudinally along missile axis at (a)  $\phi = 180^\circ$ , (b)  $\phi = 150^\circ$ , (c)  $\phi = 120^\circ$ , and (d) circumferentially at  $X/D = 4.3$ ,  $Re = 14 \times 10^6$ ,  $PR = 130$**

## **Appendix B. Hot-Gas Jet Turbulence Effects, $PR = 130$**

---

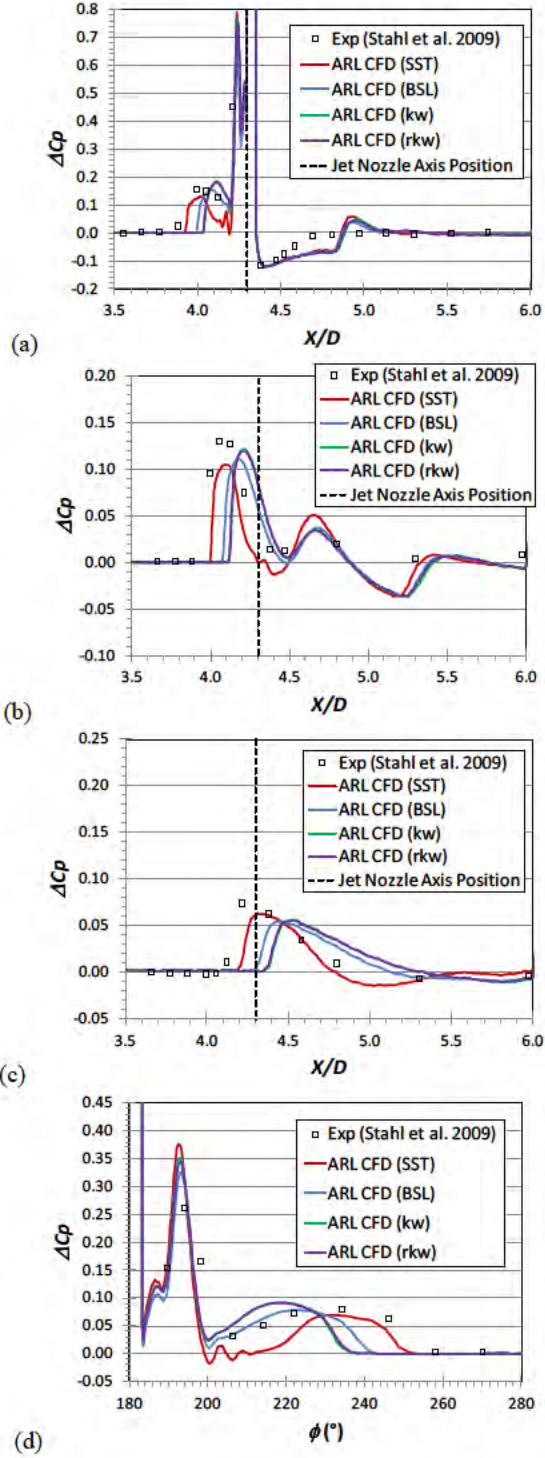


**Fig. B-1** Effect of  $k-\omega$ -based turbulence models on hot-gas jet surface pressure profiles longitudinally along missile axis at (a)  $\phi = 180^\circ$ , (b)  $\phi = 150^\circ$ , (c)  $\phi = 120^\circ$ , and (d) circumferentially at  $X/D = 4.3$ ,  $Re = 14 \times 10^6$ ,  $PR = 130$

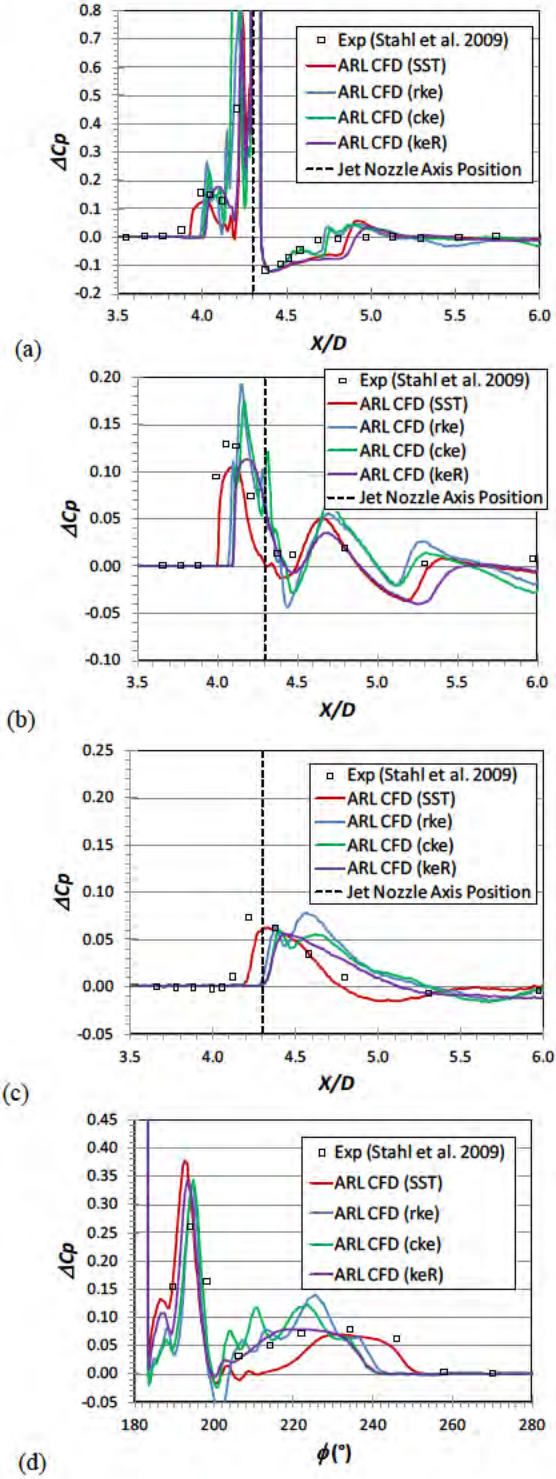


**Fig. B-2 Effect of Menter's Shear Stress Transport (SST) and  $k$ - $\epsilon$ -based turbulence models on hot-gas jet surface pressure profiles longitudinally along missile axis at (a)  $\phi = 180^\circ$ , (b)  $\phi = 150^\circ$ , (c)  $\phi = 120^\circ$ , and (d) circumferentially at  $X/D = 4.3$ ,  $Re = 14 \times 10^6$ ,  $PR = 130$**



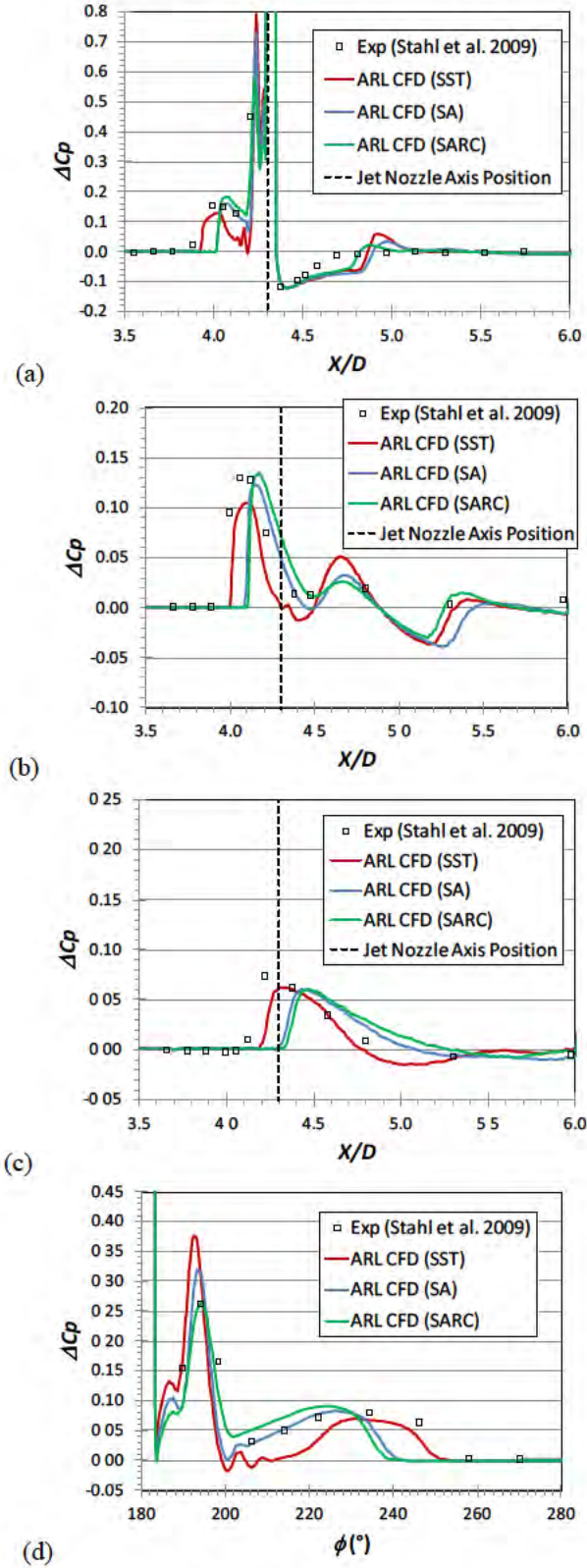


**Fig. B-3** Effect of SST and Spalart-Allmaras-based turbulence models on hot-gas jet surface pressure profiles longitudinally along missile axis at (a)  $\phi = 180^\circ$ , (b)  $\phi = 150^\circ$ , (c)  $\phi = 120^\circ$ , and (d) circumferentially at  $X/D = 4.3$ ,  $Re = 14 \times 10^6$ ,  $PR = 130$

## List of Symbols, Abbreviations, and Acronyms

---

ARL	U.S. Army Research Laboratory
BSL	Menter's baseline turbulence model
CCF	cone-cylinder-flare
CFD	computational fluid dynamics
$C_p$	pressure coefficient
$C_{p_{\text{no-jet}}}$	pressure coefficient for case with no jet injection
cke	cubic $k$ - $\varepsilon$ turbulence model
$D$	diameter of cylindrical section of missile, m
DLR	German Aerospace Center
DOD	Department of Defense
DSRC	DOD Super Computing Resource Center
$d$	jet nozzle diameter, m
$F_A$	axial force, N
$F_j$	jet thrust force, N
$F_{ji}$	jet interaction force, N
$F_{\text{no-jet}}$	normal force due to $\alpha$ without jet, N
$F_{\text{total}}$	total normal force (thrust + interaction + force due to $\alpha$ ), N
ISL	Institute of Saint-Louis
$I_t$	turbulent intensity
JI	jet interaction
$K_f$	jet force amplification factor
$K_m$	jet moment amplification factor about MRP
$K_{m(0)}$	jet moment amplification factor about missile nose
$k$	turbulent kinetic energy, $\text{m}^2\text{-s}^{-2}$
keR	Goldberg's $k$ - $\varepsilon$ - $R_t$ turbulence model

$k\omega$	standard $k$ - $\omega$ turbulence model
$l_j$	distance between missile center of gravity and jet nozzle axis, m
$l_t$	turbulent length scale, m
$M$	Mach number
$M_j$	moment about MRP induced by jet thrust force, N-m
$M_{j(0)}$	moment about missile nose induced by jet thrust force, N-m
$M_{ji}$	moment about MRP induced by jet interaction force, N-m
$M_{ji(0)}$	moment about missile nose induced by jet interaction force, N-m
MRP	moment reference point (e.g., center of gravity or jet nozzle axis location)
$PR$	jet total-to-freestream static pressure ratio, $p_{0j} / p_\infty$
$p_\infty$	freestream static pressure, Pa
$p_0$	freestream total pressure, Pa
$p_{0j}$	jet total pressure, Pa
RANS	Reynolds-averaged Navier-Stokes
$Re$	Reynolds number
$R_H$	gas constant, J/kg-K
$R_t$	undamped eddy viscosity
rke	realizable $k$ - $\varepsilon$ turbulence model
rk $\omega$	realizable $k$ - $\omega$ turbulence model
SA	Spalart-Allmaras turbulence model
SARC	Spalart-Allmaras turbulence model with rotation and curvature corrections
SST	Menter's Shear Stress Transport turbulence model
STD	standard deviation
$T_\infty$	freestream static temperature, K
$T_0$	freestream total temperature, K



$T_{0jc}$	cold-jet total temperature, K
$T_{0jH}$	hot-jet total temperature, K
$X$	axial distance along missile, m
$X_{cp}$	center of pressure location relative to missile nose, calibers
$Z$	radial distance from missile axis in pitch plane, m
$y^+$	nondimensional wall distance
$\alpha$	angle of attack, degrees
$\varepsilon$	eddy diffusivity, $\text{m}^2\text{-s}^{-1}$
$\gamma$	isentropic exponent, ratio of specific heats
$\phi$	circumferential location around missile body, $^\circ$
$\rho_\infty$	freestream gas density, $\text{kg-m}^{-3}$
$\omega$	specific dissipation, $\text{s}^{-1}$

1 (PDF)	DEFENSE TECHNICAL INFORMATION CTR DTIC OCA	1 (PDF)	NASA LANGLEY RSRCH CTR S VIKEN
2 (PDF)	DIRECTOR US ARMY RESEARCH LAB RDRL CIO LL IMAL HRA MAIL & RECORDS MGMT	3 (PDF)	NAVAIR D FINDLAY J LEE T SHAFER
1 (PDF)	GOVT PRINTG OFC A MALHOTRA	2 (PDF)	NAWCWD P CROSS R SCHULTZ
8 (PDF)	RDECOM AMRDEC L AUMAN J DOYLE S DUNBAR B GRANTHAM K KENNEDY M MCDANIEL C ROSEMA J KEENAN	1 (PDF)	AFOSR EOARD G ABATE
16 (PDF)	RDECOM ARDEC D CARLUCCI S CHUNG D CLER M DUCA L FLORIO J GRAU M HOLLIS W KOENIG A LICHTENBERG-SCANLAN G MALEJKO T RECCHIA C G STOUT W TOLEDO J TRAVAILLE E VAZQUEZ C WILSON	3 (PDF)	NSWC DAHLGREN L STEELMAN K PAMADI S KOSKI
		2 (PDF)	UNITED STATES MILITARY ACADEMY (USMA) M BENSON B VANPOPPEL
		1 (PDF)	AEROPREDICTION INC F MOORE
		1 (PDF)	ARROW TECH W HATHAWAY
		4 (PDF)	ATK B BASEGHI R DORHN S OWENS A SAIDI
		2 (PDF)	GEORGIA INST OF TECHLGY M COSTELLO J ROGERS
4 (PDF)	PM CAS M BURKE R KIEBLER P MANZ G SCHWARTZ	1 (PDF)	VILLANOVA UNIV K FOULADI
3 (PDF)	PM MAS J FOULTZ C GRASSANO D RIGOGLIOSO	1 (PDF)	MISSOURI UNIV OF SCI AND TECHLGY L DUAN
		1 (PDF)	KANSAS UNIV Z WANG

1 (PDF)	DEFENCE TECHLGY AGCY (DTA) N WILLIAMS	J MALEY B NELSON B TOPPER RDRL WML G
2 (PDF)	INSTITUTE SAINT LOUIS (ISL) C BERNER P GNEMMI	C EICHHORST C GOODEAUX M MINNICINO J SOUTH RDRL WML H
2 (PDF)	DEFENCE RSRCH AND DEV CANADA (DRDC) D CORRIVEAU N HAMEL	J NEWILL RDRL WMM J ZABINSKI RDRL WMP D LYON RDRL WMP G R BANTON
2 (PDF)	DEFENCE SCI AND TECHLGY LAB (DSTL) T BIRCH R CHAPLIN	
2 (PDF)	DEFENCE SCI AND TECHLGY ORGANIZATION (DSTO) M GIACOBELLO B WOODYATT	
35 (PDF)	DIR USARL RDRL WM P BAKER M CHEN RDRL WML P PEREGINO M ZOLTOSKI RDRL WML A W OBERLE L STROHM RDRL WML B N TRIVEDI RDRL WML C S AUBERT RDRL WML D M NUSCA RDRL WML E V BHAGWANDIN I CELMINS L FAIRFAX F FRESCONI J GARNER B GUIDOS G OBERLIN J SAHU S SILTON P WEINACHT RDRL WML F G BROWN J CONDON B DAVIS M ILG B KLINE	

INTENTIONALLY LEFT BLANK.